Journal of Theoretical Biology 595 (2024) 111966

Contents lists available at ScienceDirect

Journal of Theoretical Biology

journal homepage: www.elsevier.com/locate/yjtbi

A bulk-surface mechanobiochemical modelling approach for single cell migration in two-space dimensions

David Hernandez-Aristizabal [a,b], Diego-Alexander Garzon-Alvarado [a], Carlos-Alberto Duque-Daza [a], Anotida Madzvamuse [c,d,e,f,*]

[a] Universidad Nacional de Colombia, Department of Mechanical and Mechatronics Engineering, Bogotá, Colombia
[b] Aix-Marseille Univ, CNRS, ISM, Marseille, France
[c] University of British Columbia, Department of Mathematics, 1984 Mathematics Road, Vancouver, V6T 1Z2, British Columbia, Canada
[d] University of Pretoria, Department of Mathematics, Pretoria, South Africa
[e] University of Johannesburg, Department of Mathematics, Johannesburg, South Africa
[f] University of Zimbabwe, Department of Mathematics and Computational Science, Mt Pleasant, Harare, Zimbabwe

ARTICLE INFO

Keywords:
Bulk-surface partial differential equations
Bulk-surface reaction–diffusion
Bulk-surface finite element method
ALE-moving mesh methods
Cell migration
Cell motility
Mechanobiochemical modelling
Moving-mesh method
Bulk-surface moving-mesh finite element method (BS-MFEM)

ABSTRACT

In this work, we present a mechanobiochemical model for two-dimensional cell migration which couples mechanical properties of the cell cytosol with biochemical processes taking place near or on the cell plasma membrane. The modelling approach is based on a recently developed mathematical formalism of evolving bulk-surface partial differential equations of reaction–diffusion type. We solve these equations using finite element methods within a moving-mesh framework derived from the weak formulation of the evolving bulk-surface PDEs. In the present work, the cell cytosol interior (bulk) dynamics are coupled to the cell membrane (surface) dynamics through non-homogeneous Dirichlet boundary conditions. The modelling approach exhibits both directed cell migration in response to chemical cues as well as spontaneous migration in the absence of such cues. As a by-product, the approach shows fundamental characteristics associated with single cell migration such as: (i) cytosolic and membrane polarisation, (ii) actin dependent protrusions, and (iii) continuous shape deformation of the cell during migration.

Cell migration is an ubiquitous process in life that is mainly triggered by the dynamics of the actin cytoskeleton and therefore is driven by both mechanical and biochemical processes. It is a multistep process essential for mammalian organisms and is closely linked to a vast diversity of processes; from embryonic development to cancer invasion. Experimental, theoretical and computational studies have been key to elucidate the mechanisms underlying cell migration. On one hand, rapid advances in experimental techniques allow for detailed experimental measurements of cell migration pathways, while, on the other, computational approaches allow for the modelling, analysis and understanding of such observations. The bulk-surface mechanobiochemical modelling approach presented in this work, set premises to study single cell migration through complex non-isotropic environments in two- and three-space dimensions.

1. Introduction

Cell motility is a phenomenon that occurs in every stage of life. It is a cyclic multi-step process in the development and maintenance of multi-cellular organisms. It consists of actin-dependent protrusions at the cell leading edge, integrin-mediated adhesions to the extracellular matrix, and acto-myosin-driven contractions of the cell (Alberts et al., 2015; Seetharaman and Etienne-Manneville, 2020; Hobson and Stephens, 2020; Yamada and Sixt, 2019). Cells have a remarkable ability to sense both physical and chemical signals that guide them to navigate through complex environments in a process known as cell migration. This process plays a pivotal role in embryonic development (Uriu et al., 2014), wound healing (Morales, 2007), immune response (Othmer, 2019) and cancer metastasis (Warner et al., 2019). Cell migration is a product of the interplay between the cytoskeleton (specifically the actin cytoskeleton) and several molecules and structures such as myosin motors and focal adhesions (Othmer, 2019; Seetharaman and

* Corresponding author at: University of British Columbia, Department of Mathematics, 1984 Mathematics Road, Vancouver, V6T 1Z2, British Columbia, Canada.
E-mail addresses: david.hernandez-aristizabal@univ-amu.fr (D. Hernandez-Aristizabal), dagarzona@unal.edu.co (D.-A. Garzon-Alvarado), caduqued@unal.edu.co (C.-A. Duque-Daza), am823@math.ubc.ca (A. Madzvamuse).

https://doi.org/10.1016/j.jtbi.2024.111966
Received 26 June 2024; Received in revised form 1 October 2024; Accepted 7 October 2024
Available online 16 October 2024

Etienne-Manneville, 2020). The actin cytoskeleton is composed of a cross-linked array of actin filaments (F-actin), the polymeric form of actin (G-actin), and associated proteins (proteins that interact with both G-actin and F-actin) (Shah and Keren, 2013; Othmer, 2019; Alberts et al., 2015; Ridley et al., 2003; Seetharaman and Etienne-Manneville, 2020).

In the last few decades research studies have explored mathematical models to help elucidate mechanisms underpinning intercellular dynamics (Buttenschön and Edelstein-Keshet, 2020). Some of them describe cell density in a continuum medium, e.g. Murray (2002, 2003), Bartha and Eftimie (2022) and Koppenol et al. (2017), where diffusive terms account for random migration, advective terms for directed migration and reactive terms for proliferation, death and other phenomena. Other models consider cells as particles that follow prescribed rules based on biological observations, such as (Harris, 2017; Chen et al., 2018b; Escribano et al., 2019; Chen et al., 2020b; González-Valverde et al., 2016; Gonçalves and Garcia-Aznar, 2021; Ahmed et al., 2023; Farmer and Harris, 2023). However, these studies fail to take into account important morphological (e.g. geometrical) properties of cells and their environments which influence cell migration. For instance, it has been demonstrated that cell shape impacts traction stress (Rape et al., 2011), the speed of collective cell migration under heat stress (Chen et al., 2020a), and cell development (McBeath et al., 2004). Other models directly study the interactions and activities of chemicals within the intra and extracellular domains as well as on the membrane (Holmes et al., 2017; Gonçalves and Garcia-Aznar, 2021). These models, that consider each cell as a separate geometric entity, can take into account the morphological changes, see for example (Alt and Tranquillo, 1995; Stéphanou and Tracqui, 2002; Fuhrmann et al., 2007; Mori et al., 2008; Neilson et al., 2011; Elliott et al., 2012; Séguis et al., 2012; Aubry et al., 2014; Cheng and Othmer, 2016; Camley et al., 2017; Campbell et al., 2017; Harris, 2017; Moure and Gomez, 2017; Zhao et al., 2017; Chen et al., 2018a; Cusseddu et al., 2019; Moure and Gomez, 2019; Peng et al., 2021, 2023; Link et al., 2024).

In addition, in recent years, important works have been carried out on the description of the nature of the biochemical species through compartmentalised models where different molecular species reside in the cytosol as well as on the cell membrane. This family of bio-molecular proteins is known as Rho GTPases, which exist in two forms, active states residing on the cell membrane and inactive states (also known as cytosolic proteins) residing in the cytosol (Olayioye et al., 2019). The biomolecular spatiotemporal interactions have been described by bulk-surface models where one set of species follows a surface partial differential equation (PDE) and another set follows a bulk PDE. Both systems of PDEs posed on different geometries are usually coupled through mixed Robin-type boundary conditions (Cusseddu et al., 2019; Elliott et al., 2012; Madzvamuse and Chung, 2016b,a). These new models known as bulk-surface reaction–diffusion systems have been shown to produce spatiotemporal dynamics similar to those observed experimentally. In Rätz and Röger (2014), Rätz (2015), Madzvamuse and Chung (2016b) and Madzvamuse and Chung (2016a), necessary conditions for the emergence of Turing patterns are derived for bulk-surface reaction–diffusion systems on stationary and evolving domains. Interestingly, the classical condition of long-range inhibition and short-range activation as a classical paradigm for pattern formation is substantially relaxed. In Giese et al. (2015), it is shown that stretched regions where protrusions occur act as negative feedbacks limiting the aggregation of the species. For the interested reader, further work on bulk-surface cell polarisation models can be found in Diegmiller et al. (2018), Miller et al. (2022), Cusseddu et al. (2019) and Elliott et al. (2017).

Our approach is a substantial generalisation of the bulk-surface PDE formalism whereby we consider each cell as a separate geometric entity whose evolution law (modelling the actin cytoskeleton displacements) for its migration is driven by both the mechanical properties and the biochemical processes. This allows us to encode and therefore model, naturally, some of key biophysical features of single as well as collective cell migration such as (i) the biochemical interplay among different molecules in the extracellular matrix, on the membrane and in the cytosol and (ii) the mechanical response of the cytoskeleton and the membrane as a consequence of the biochemical dynamics.

The biochemical system must be capable of generating stable and polarised states, such as those emerging from excitable systems (Bhattacharya and Iglesias, 2016; Allard and Mogilner, 2013). An example of this is the wave-pinning model (Mori et al., 2008; Camley et al., 2017; Cusseddu et al., 2019). Another option is to consider Turing instabilities (Goehring and Grill, 2013), as in the case of Meinhardt's model of cell polarisation (Meinhardt, 1999; Neilson et al., 2011; Elliott et al., 2012; Campbell et al., 2017). An alternative approach, presented in Cheng and Othmer (2016), involves a biologically motivated model where the variables directly correspond to biochemical species, allowing for a more precise comparison with experimental data. The drawback of this approach is that it is computationally more expensive than using mathematical models that reproduce specific behaviours. This is a consequence of the large number of variables necessary in biologically-motivated models. For instance, the Cheng and Othmer (2016) model considers more than twenty variables while Meinhardt's model only considers three.

Regarding the mechanical system, the cytoskeleton plays a major role in cell migration. The mechanical properties are highly dependent on actin filaments, microtubules and intermediate filaments. The rigidity of the cell is given by the amount and organisation of actin filaments (Han et al., 2022). In addition, changes on the rigidity of the extracellular matrix lead to changes in cell rigidity (Espina et al., 2021). Microtubules can resist compressive forces and work as anchorage structures when attached to focal adhesions. Intermediate filaments provide structural integrity and viscoelastic properties (Espina et al., 2021). Thus, we see that the mechanics within cells are highly dynamic since the elastic and viscoelastic properties depend on the density and organisation of the cytoskeleton.

When modelling the mechanical behaviour, it is usually assumed that inertial forces are negligible with respect to elastic and viscoelastic forces (Lewis and Murray, 1991). Therefore, the system is considered to be in equilibrium. Such equilibria are defined by the shear–stress relation of the media (which could be elastic, viscous or viscoelastic), growth and surface forces. Growth forces are derived from the biochemical activities and can be applied both on the surface (Neilson et al., 2011; Elliott et al., 2012; Campbell et al., 2017) and in the bulk (Stéphanou and Tracqui, 2002; Murphy and Madzvamuse, 2020; Madzvamuse and George, 2013). Surface forces comprise both external stimuli and membrane forces as a function of the mean-curvature vector (Neilson et al., 2011; Elliott et al., 2012; Campbell et al., 2017; Stéphanou and Tracqui, 2002).

An interesting and alternative approach has been developed in Chen et al. (2018b) where cell mechanics is modelled by means of springs. It is considered that a predefined number of links defines the cell cytoskeleton. The movement is governed by the balancing of spring and chemotactic forces and random movements. This formalism has been extended to consider cell–cell and cell-barrier interactions (Peng et al., 2021) and focal adhesions (Peng et al., 2023).

In this paper, we implement a computational framework that models fundamental migration properties such as: (i) spontaneous and chemotactic membrane polarisation, (ii) cytosolic polarisation, and (iii) actin-dependent protrusion. The framework considers a bulk-surface reaction–diffusion system to model the biochemical dynamics and the mechanical equilibrium of growing domains. For illustrative purposes, we present a numerical example employing Meinhardt's (1999) model for cell orientation on the membrane and a linear diffusion-depletion model for cytosolic polarisation. Furthermore, we assume that cytosolic diffusion occurs on significantly larger timescales than the membrane diffusion. This can be justified by experimental measurements of membrane and cytosolic diffusion coefficients. For instance, in *Escherichia*

coli, surface diffusion coefficients on the membrane have been found to be around 30 times lower than those in the bulk cytosol (Elowitz et al., 1999; Nenninger et al., 2010, 2014). In addition, we simplify the mechanical model to the elastic case, and consider only the expansive and contractile forces dependent on cytosolic dynamics and on morphological properties. The proposed computational approach is based on a novel bulk-surface moving-mesh finite element method for semi-linear parabolic partial differential equations (Cusseddu et al., 2019; Cusseddu and Madzvamuse, 2022; Madzvamuse and Chung, 2016b). We note that our computational approach does not consider fitting the model to experimental data; therefore, the parameters that we use are defined to demonstrate the ability of the model to exhibit experimentally observed cell migration pathways. Implementing model fitting and parameter estimation for the mechanobiochemical model as proposed is currently beyond this study due to the lack of detailed experimental datasets both for the mechanical properties and the biochemical processes as well as the complex nature of coupling of different properties and processes on a moving domain.

Our paper is therefore organised as follows. In Section 2, we present the bulk-surface mechanobiochemical model for two-dimensional cell migration which is based on biological observations. Section 3 deals with the exposition of the bulk-surface moving-mesh finite element method applied to the mechanobiochemical model. The proposed numerical method is validated in Section 4. Cell migration pathways are exhibited in Section 5. In Sections 6 and 7, we discuss the implications of the bulk-surface moving-mesh finite element method applied to a mechanobiochemical model for cell migration and conclude our study by describing open problems in computational modelling of cell migration in multi-dimensions.

2. Formulating the mechanobiochemical model

In this section, we will present a biological description of cell migration as a starting-point of the mechanobiochemical model. We will describe fundamental biological features and some examples of how these occur. We will then proceed to formulate the mechanobiochemical model based on the general biophysical principles which govern single cell dynamics with appropriate mathematical modelling assumptions.

2.1. Biological motivation

A key feature of migration is the ability of cells to polarise the activity of the cytoskeleton towards a biased direction. This polarised state is characterised by high concentrations of actin filaments at the leading edge and high concentrations of myosin II at the rear edge (Alberts et al., 2015). High concentrations of actin filaments push the membrane, generating protrusions, while high concentrations of myosin II pull the cytoskeleton, producing contractility. Moreover, new focal adhesions are constantly nucleated at the leading edge, while at the same time, the ones at the rear are either broken or disassembled (Ridley et al., 2003; Seetharaman and Etienne-Manneville, 2020). Fig. 1 illustrates the organisation of the cell during migration.

Although this might sound simple, the machinery for cell polarisation and migration is highly complex. It comprises biochemistry, mechanics and their cross-communication. For instance, in the case of directed cell migration of *Dictyostelium*, cell surface receptors coupled to G-proteins (GPCRs) trigger different signalling cascades that lead to the formation of protrusions (Vorotnikov, 2011), after being activated by extracellular binding molecules. For example, activated GPCRs switch on some membrane proteins of the Ras superfamily and Phosphoinositide 3-kinase (PI3K). After that, other proteins promote the accumulation of Phosphatidylinositol (3,4,5)-trisiphosphate (PIP3) at the leading edge. Then, PIP3 recruits downstream proteins that enhance the activity of the actin network at the plasma-membrane cortex of the leading edge (Artemenko et al., 2014). As a result, this

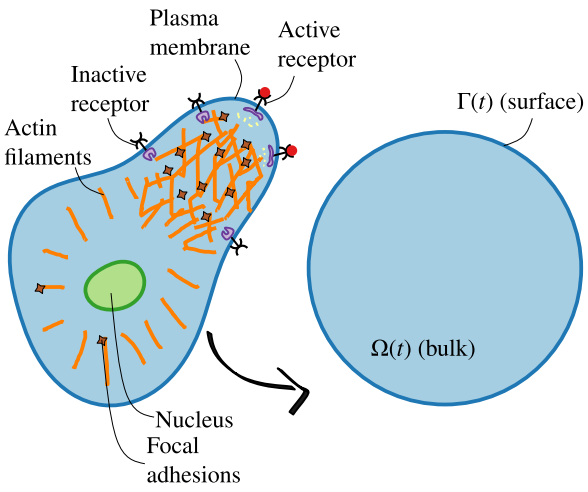

Fig. 1. Schematic representation of the cell during migration to the left. To the right, domain simplification for the mathematical model.

activity may push the membrane (a mechanical response) extending filopodia, lamellipodia or invadopodia (Othmer, 2019). On the other hand, the mechanical properties of the environment can be transduced into biochemical stimuli affecting the intracellular molecular interplay—a process called mechanotransduction (Seetharaman and Etienne-Manneville, 2020). In addition, there is no unique signalling pathway controlling cell migration. Instead, cells have several redundant and antagonist signalling pathways (Ridley et al., 2003; Krause and Gautreau, 2014; Devreotes and Horwitz, 2015).

Given such complexity, modelling this phenomenon requires a large amount of data (regarding the interactions inside and outside the cell) or an understanding of the possible underlying mechanisms. In Onsum and Rao (2009), the authors indicated bottom-up and top-down approaches. In the former, a set of proteins and their interactions are defined based on experimental observations, and mathematical models are hence established such that each variable directly represents a specific molecule and each term describes real biochemical reactions. The consistency of the models is tested by comparing its evolution with experimental observations. In addition, mathematical analysis (e.g. stability) might elucidate unknown features of the underlying mechanism. In the top-down approach, a general mechanism (e.g. Turing instability) able to respond in a similar manner as what has been observed experimentally is assumed. These models enable to hypothesise about the nature of the underlying molecules that drive the biological phenomenon.

The computational framework that we propose here can deal with both type of approaches. Yet, for the sake of simplicity, we shall consider the top-down one. Therefore, we will aim to reproduce the behaviour of the biological system without directly modelling each interacting molecule.

Let us start with the membrane dynamics. As mentioned in Rappel and Edelstein-Keshet (2017), Onsum and Rao (2009) and Meinhardt's (1999) model for cell orientation may be a suitable candidate to generate polarised states. It is one of the so called local excitation and global inhibition (LEGI) models. A key feature of these models is the difference between the diffusion rates of activators and inhibitors—those of the former are much lower than those of the latter. Within the cell, it is common that active membrane proteins diffuse more slowly than their inactive counterparts which are generally cytosolic molecules (Rappel and Edelstein-Keshet, 2017). This feature is what accounts for local excitation and global inhibition. Meinhardt's (1999) model has the following characteristics: (i) a space-dependent reaction rate that accounts for external cues; (ii) an autocatalytic activator that amplifies the deviations from the mean; (iii) a global inhibitor that restricts the

amplified activator to a few regions; and (iv) a local inhibitor that destabilises steady patterns and allows the emergence of a spatially inhomogeneous solution that results in the reorientation of the cell leading edge. Thus, we will consider: (i) a set of proteins that transduce external cues into internal ones; (ii) a set of proteins that activate supportive and antagonist pathways allowing them to amplify the external cues and accumulate at the leading edge; (iii) a set of homogeneously distributed proteins that prevent the amplification of the external cues at the rear; and (iv) a set of proteins mainly located at the leading edge able to breakdown the amplification which permits the system to reorient if necessary. For this exposition, we chose to consider all the variables belonging to the signal amplification model as surface entities for simplicity. This choice is reasonable since in Meinhardt's model, the fast diffusing species – which represents the bulk proteins – is homogeneous due to the timescale difference with the other species. A similar assumption has been done in Diegmiller et al. (2018) and Cusseddu and Madzvamuse (2022), using the wave-pinning model. In both cases, the authors considered the bulk proteins as homogeneously distributed and showed that the proposed approximation was accurate when the bulk diffusion coefficient was considered larger. This is also consistent with experimental measurements; for instance, in *Escherichia coli*, the bulk proteins diffuse 30 times faster than membrane proteins (Elowitz et al., 1999; Nenninger et al., 2010, 2014).

The polarisation of the membrane then leads to the polarisation of the cytoskeleton. This means that there is a flow of information between these two domains. The first assumption of our model here will be to consider that this information goes only from the plasma-membrane to the cytoskeleton—we assume that while the dynamics on the membrane affect the dynamics in the cytoskeleton, the former are independent of the latter. As a second assumption, we will simplify the cytoskeleton dynamics to the assembling and disassembling of actin filaments. Although the cytoskeleton is composed of microtubules, intermediate filaments and actin filaments (Alberts et al., 2015), cell migration is mainly associated with the dynamics of the actin network (Schaks et al., 2019). In fact, computational models in the literature usually neglect the activity of microtubules and actin filaments (Alt and Tranquillo, 1995; Stéphanou and Tracqui, 2002; Neilson et al., 2011; Madzvamuse and George, 2013). A third assumption will be that the concentration of the actin network near the plasma-membrane is proportional to the one on the membrane. This is a hypothetical assumption to be verified or refuted experimentally. It is also mathematically important since it allows us to use Dirichlet boundary conditions which directly indicate the concentration of the bulk variables on the surface. Lastly, we will consider a simple diffusion-depletion model for the general actin-network activity. Although this model simplifies the actomyosin system, it allows us to reproduce a polarised pattern in the bulk as a downstream effect of the membrane polarisation.

Finally, with the polarised plasma-membrane and cytoskeleton, we can consider the mechanical response. Here, the mechanics will be coupled to the biochemistry by means of forces driven by the concentration of the chemical species. The biochemistry will also be affected by the displacements through the material velocity. First, let us simplify the mechanics of the cytoskeleton by considering linear elastic deformation and plane stress behaviour (Irgens, 2008). Furthermore, let us consider that no elastic energy is accumulated and, thus, the cell does not recover its shape after each step of deformation. This is following the work in Zhao et al. (2017) where the authors acknowledged that cell cytoskeleton and adhesive structures are rapidly reconstructed—this observation allows us to refer to the material model as elastic without energy accumulation instead of perfectly plastic. Second, let us couple the biochemical dynamics by considering a bulk concentration-dependent isotropic expansion. As actin filaments grow, they apply pressure to both the plasma membrane and focal adhesions (Othmer, 2019). We will consider that this growth translates into mechanical stress along the filament by the linear form: $\sigma_{\text{fil}} = E\varepsilon_{\text{fil}}$, where ε_{fil} is the strain or deformation along the filament induced by the activity of the actin network and E is the modulus of elasticity that linearly relates the stress and the strain (Irgens, 2008). Given that the actin network is highly cross-linked, we take it as a homogeneous and isotropic material; thus, following the plane-stress strain–stress relation (Ferreira, 2009) and considering no induced shear strain, the mechanical stress now reads: $(\sigma_a)_{11} = (\sigma_a)_{22} = (E/(1-\nu))\varepsilon_a$ and $(\sigma_a)_{12} = (\sigma_a)_{21} = 0$, where $\boldsymbol{\sigma}_a$ and ε_a are respectively the stress tensor (with components $(\sigma_a)_{ij}$, $i,j \in \{1,2\}$) and the deformation induced by the actin network. As a third consideration, we will take the equation for the area control presented in Neilson et al. (2011). It describes the evolution of a Lagrange multiplier that monitors the growth of the area. We will then consider isotropic contraction with the stress tensor: $\boldsymbol{\sigma}_c$ such that $(\sigma_c)_{11} = (\sigma_c)_{22} = (E/(1-\nu))\varepsilon_c$ and $(\sigma_c)_{12} = (\sigma_c)_{21} = 0$, where ε_c is the deformation induced by the isotropic contraction, which depends on the evolution of the area control equation in Neilson et al. (2011). We will also include membrane tension as a traction on the boundary proportional to the mean curvature vector, as previously done in Neilson et al. (2011) and Elliott et al. (2012). Finally, similarly to Zhao et al. (2017) we will include the effect of focal adhesions as elastic supports.

Given the mentioned assumptions, we consider a two-dimensional evolving domain $\Omega(t) \subset \mathbb{R}^2 \times [0,T_f]$ with a continuously deforming curvilinear boundary $\Gamma(t) \subset \mathbb{R}^2 \times [0,T_f]$, representing an evolving curve in $\mathbb{R}^2$. For simplicity, we ignore the nucleus and its dynamics, $\Omega(t)$ only represents the cytoplasm in the absence of the nucleus, see Fig. 1. $\Gamma(t)$ is assumed to be a sharp-interface approximation of the plasma membrane. On $\Gamma(t)$, we model the signal amplification using the model of Meinhardt (1999). In $\Omega(t)$, we model the actin-cytoskeleton dynamics by considering a linear diffusion-depletion system. Finally, we include elastic deformation as a response of the actin-cytoskeleton dynamics, shape changes and membrane tension.

2.2. Formulating a surface reaction–diffusion system on the plasma membrane $\Gamma(t)$

Let us start defining the surface operators necessary to yield the reaction–diffusion equation on evolving curves. As in Dziuk and Elliott (2007, 2013) and Barreira et al. (2011), consider an orientable curve $\Gamma(t) \subset \mathbb{R}^2 \times [0,T_f]$, which can be represented by a level set function $d(\boldsymbol{x},t) : \mathbb{R}^2 \times [0,T_f] \to \mathbb{R}$. Here, $d(\boldsymbol{x},t)$ is the signed distance from $\boldsymbol{x}$ to $\Gamma(t)$ at time t, with T_f the final time. Thus, $\Gamma(t) = \{\boldsymbol{x} \in \mathbb{R}^2 : d(\boldsymbol{x},t) = 0\}$, and the outward unit normal vector can be written as: $\boldsymbol{n}(\boldsymbol{x},t) = \nabla d(\boldsymbol{x},t)/\|\nabla d(\boldsymbol{x},t)\|$.

Let us now define a neighbourhood of $\Gamma(t)$ of size δ as the open subset $\mathbb{R}^2 \supset \mathcal{U}(t) = \{\boldsymbol{x} \in \mathbb{R}^2 : d(\boldsymbol{x},t) < \delta\}$. We now compute the surface gradient of a function $f(\boldsymbol{x},t) : \Gamma(t) \times [0,T_f] \to \mathbb{R}$, by defining an extension of this function to $\hat{f}(\boldsymbol{x},t) : \mathcal{U}(t) \times [0,T_f] \to \mathbb{R}$ as for example:

$$\hat{f}(\boldsymbol{x},t) = \begin{cases} f(\boldsymbol{x},t), & \text{if } d(\boldsymbol{x},t) = 0, \\ f\left(\boldsymbol{x} - d(\boldsymbol{x},t)\boldsymbol{n}(\boldsymbol{x},t),t\right), & \text{otherwise.} \end{cases}$$

Then, the surface gradient of f is given by: $\nabla_{\Gamma(t)} f(\boldsymbol{x},t) = \nabla \hat{f}(\boldsymbol{x},t) - \nabla \hat{f}(\boldsymbol{x},t) \cdot \boldsymbol{n}(\boldsymbol{x},t)\boldsymbol{n}(\boldsymbol{x},t)$. Furthermore, the Laplace-Beltrami operator is: $\Delta_{\Gamma(t)} f(\boldsymbol{x},t) = \nabla_{\Gamma(t)} \cdot \nabla_{\Gamma(t)} f(\boldsymbol{x},t)$ (Dziuk and Elliott, 2007, 2013).

Having defined the surface gradient and the Laplace-Beltrami operator, let us continue with the derivation of the reaction–diffusion system on evolving surfaces. Let $a_k(\boldsymbol{x}(t),t)$, with $\boldsymbol{x}(t) \in \Gamma(t)$ and $k \in \mathbb{N}$, denote the kth molecular species resident on $\Gamma(t)$ whose dynamics follow a reaction–diffusion behaviour on $\Gamma(t)$; the kth equation is given by (Barreira et al., 2011; Frittelli et al., 2018; Dziuk and Elliott, 2007, 2013):

$$\partial^\bullet a_k + a_k \nabla_{\Gamma(t)} \cdot \mathbf{v} - d_k \Delta_{\Gamma(t)} a_k = f_k(\boldsymbol{a}), \tag{1}$$

where $\boldsymbol{a}$ denotes the vector of the molecular species; d_k is the constant diffusion coefficient of the kth species; and $\mathbf{v}$ is the material velocity defined as: $\mathbf{v} = d\boldsymbol{u}/dt$, where $\boldsymbol{u}$ represents the actin cytoskeleton

displacements which satisfy the momentum equation described below (Murphy and Madzvamuse, 2020; George et al., 2013), Eq. (13). In the above, we have assumed that the flux of each species follows Fick's law (Murray, 2002; Turing, 1952). The reaction kinetics are defined by f_k which can take the form of excitable systems, Turing instability models or experimentally driven models (Juma, 2019). In addition, the material derivative is defined by: $\partial^\bullet a_k = \frac{\partial a_k}{\partial t} + \mathbf{v}\cdot\nabla a_k$, where the material velocity $\mathbf{v}$ describes the changes in the actin cytoskeleton displacements, denoted by $\boldsymbol{u}$ above. The first term at the left-hand side of Eq. (1) is the material derivative of a_k; the second term corresponds to the dilation due to the growth of the domain; and the third corresponds to the diffusion. The term at the right-hand side represents nonlinear reaction kinetics, and this is the only term in which interactions between the k-species take place.

In the present work, we will consider as an example the reaction kinetics of Meinhardt (1999) for cell orientation. These have been used in previous studies to demonstrate the ability of the model to reproduce dynamics similar to those of cell migration (Neilson et al., 2011; Elliott et al., 2012; Campbell et al., 2017). Thus, for $k = 1, 2, 3$, the system of equations is postulated as follows:

$$\partial^\bullet a_1 + a_1\nabla_{\Gamma(t)}\cdot\mathbf{v} - d_1\Delta_{\Gamma(t)}a_1 = \gamma f_1(a_1,a_2,a_3) \qquad \text{on } \Gamma(t), \tag{2}$$

$$\partial^\bullet a_2 + a_2\nabla_{\Gamma(t)}\cdot\mathbf{v} - d_2\Delta_{\Gamma(t)}a_2 = \gamma\left(k_2\hat{a}_1 - r_2a_2\right) \qquad \text{on } \Gamma(t), \tag{3}$$

$$\partial^\bullet a_3 + a_3\nabla_{\Gamma(t)}\cdot\mathbf{v} - d_3\Delta_{\Gamma(t)}a_3 = \gamma\left(k_3a_1 - r_3a_3\right) \qquad \text{on } \Gamma(t), \tag{4}$$

with:

$$f_1(a_1,a_2,a_3) = \frac{s_e\left(\frac{a_1^2}{a_2}+k_1\right)}{(s_3+a_3)(1+s_1a_1^2)} - r_1a_1, \tag{5}$$

for $t \in [0, T_f]$, with initial conditions: $a_k(\boldsymbol{x}(0), 0)$. It must be noted that since $\Gamma(t)$ is a closed curve, its boundary is empty; and hence, no boundary conditions are required. In Eqs. (2) and (4)–(6), a_1 is the autocatalytic activator, and a_2 and a_3 are respectively the global and local inhibitors; $\hat{a}_1$ is the average value of a_1; d_1, d_2 and d_3 are diffusion coefficients; γ is the strength of the reaction; k_1, k_2 and k_3 are the production rates of the activator and the global and the local inhibitor, respectively; s_1 is the saturation rate of the local catalysis, and s_3 is the Michaelis–Menten constant; r_1, r_2 and r_3 are respectively the consumption rates of the activator and the global and local inhibitors; and s_e is the signalling parameter which captures chemotactic gradients and noise, therefore, it is space-dependent (Meinhardt, 1999)—this term can be viewed as the activity of membrane receptors.

Notice that when $a_2(\boldsymbol{x}(t), t)$ is spatially constant, the diffusive term in Eq. (3) vanishes. Additionally, since $\hat{a}_1$ is constant in space, the reaction term also becomes space-independent when $a_2(\boldsymbol{x}(t), t)$ is space-independent. Therefore, if $a_2(\boldsymbol{x}(0), 0)$ is constant in space, Eq. (3) can be rewritten without the diffusive term as (Elliott et al., 2012):

$$\partial^\bullet a_2 + a_2\nabla_{\Gamma(t)}\cdot\mathbf{v} = \gamma\left(k_2\hat{a}_1 - r_2a_2\right) \text{ on } \Gamma(t). \tag{6}$$

Meinhardt (1999) proposed s_e as:

$$s_e(\boldsymbol{x}(t)) = r_1\left(1+\eta_s\cos\left(2\pi\frac{\text{arc}(\boldsymbol{x}(t)-\boldsymbol{x}_c(t))}{|\Gamma(t)|}\right)\right)\left(1+\eta_nRND\right), \tag{7}$$

where $\text{arc}(\boldsymbol{x}(t)-\boldsymbol{x}_c(t))$ is the distance from $\boldsymbol{x}(t) \in \Gamma(t)$ to $\boldsymbol{x}_c(t)$. Here, $\boldsymbol{x}_c(t)$ is the closest point on $\Gamma(t)$ to an external source indicating the directional asymmetry; η_s and η_n are respectively the strength of a signal coming from a specific point outside the cell and the random noise; $|\Gamma(t)|$ is the size (the perimeter) of the membrane at time t; and RND refers to a random number.

This function has two main drawbacks: it does not model the switchable behaviour of membrane receptors and the strength of the signal does not depend on the distance to the source. As a response, Neilson et al. (2011) proposed a kinetic system that models the activity of the membrane considering receptor occupancy. However, Wang and Irvine (2013) indicated that receptor occupancy gradients are a consequence of the concentration gradient along the membrane of a chemoattractant. This observation allows us to avoid the need of modelling the membrane-receptor kinetics. Instead, we modify Eq. (7) only to depend on the distance to the source. This leads to the following function:

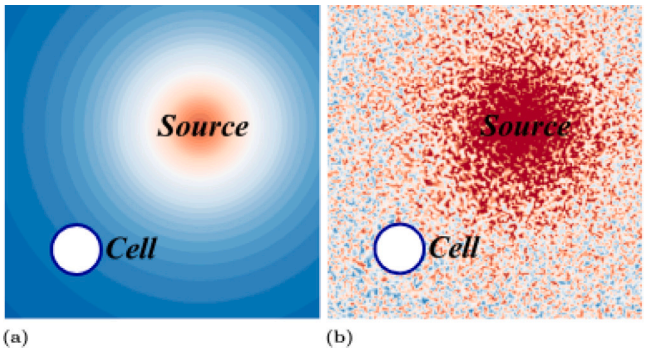

Fig. 2. External signal s_e around a circular cell with (a) $\eta_n = 0$ and (b) $\eta_s \neq 0$. The blue and red colours respectively indicate low and high concentration.

$$s_e(\boldsymbol{x}(t)) = r_1\left(1+\eta_s\frac{|\Gamma(t)|}{|\Gamma(t)|+d(\boldsymbol{x}(t),t)^2}\right)\left(1+\eta_nRND\right), \tag{8}$$

where $d(\boldsymbol{x}(t), t)$ is the distance from $\boldsymbol{x}(t) \in \Gamma(t)$ to the signalling point, which can be outside $\Gamma(t)$. Fig. 2 illustrates the s_e in space and shows how the receptor occupancy on the membrane would behave.

2.3. Formulating a bulk reaction–diffusion equation in the cytoplasm $\Omega(t)$ for actin cytoskeleton activity

The polarisation on the membrane leads to the activation of downstream signalling pathways that trigger the reorganisation of the cytoskeleton. In a general case, the dynamics of the bulk can be modelled as follows. Let a_j denote the jth cytoplasmic variable; the reaction–diffusion system coupled to the surface dynamics is given by (Madzvamuse et al., 2005):

$$\frac{\partial a_j}{\partial t} + \nabla\cdot(\mathbf{v}a_j) = d_j\Delta a_j + g_j(\boldsymbol{a}) \qquad \text{in } \Omega(t), \tag{9}$$

$$\mu d_j\frac{\partial a_j}{\partial \boldsymbol{n}} = g_j^\Gamma(\boldsymbol{a}) \qquad \text{on } \Gamma(t), \tag{10}$$

where μ is a positive parameter; g_j represents the nonlinear reaction kinetics in the bulk; and g_j^Γ the coupling dynamics from the surface to the bulk.

For the present work, we shall use a simplified version of Eqs. (9) and (10). We can first reduce the actin-network to one variable representing the actin concentration which is the growth driving force. We can also consider that polarisation beneath the membrane is proportional to that on the membrane itself. Although these assumptions neglect the intermediate interactions between the membrane and the bulk variables, they reproduce the polarising effect from the external signal to the cell membrane to the cell cytoskeleton. Hence, only one bulk variable is considered representing the actin-network in the cytoplasm, say a_b. For the actin-network dynamics, we can consider a linear diffusion-depletion system with Dirichlet boundary conditions dependent on the activity on the membrane for polarisation. This is equivalent to say that $g_b = G_b - C_ba_b$, where G_b and C_b are respectively the rates of decay and production of actin network. In addition, in Eq. (10), $\mu = 0$ and $g_b^\Gamma = a_b - a_3$, where a_3 comes from the surface model. With this boundary condition, we directly reproduce the polarisation of the actin cytoskeleton as a result of the polarisation of upstream regulators. We continue the model simplification by further considering that a_b rapidly reaches a steady state after any perturbation on the boundary. This yields:

$$0 = d_b\Delta a_b - C_ba_b + G_b \qquad \text{in } \Omega(t), \tag{11}$$

$$a_b = a_3 \qquad \text{on } \Gamma(t), \tag{12}$$

where d_b and C_b are respectively the diffusion coefficient and the decay rate of a_b, and G_b is constant production rate of a_b. As can be seen, the left-hand-side of Eq. (9) is neglected.

2.4. Formulating the mechanical model for the cytoskeleton dynamics in the cytoplasm

As mentioned above, we will consider an elastic model with isotropic expansion and contraction due to the actin network and the area change, respectively; adhesion to the substratum as homogeneously distributed elastic supports (Zhao et al., 2017); and surface forces due to membrane tension (Neilson et al., 2011; Campbell et al., 2017; Elliott et al., 2012). Hence, the momentum equation (Stéphanou et al., 2004; George et al., 2013; Madzvamuse and George, 2013; Murphy and Madzvamuse, 2020) reads: find the displacement field $\boldsymbol{u}(\boldsymbol{x}, t) \in C^2(\Omega, [0, T_f])$ such that:

$$\nabla \cdot (\boldsymbol{\sigma}(\nabla \boldsymbol{u}) - \boldsymbol{\sigma}_a(a_b) + \boldsymbol{\sigma}_c(\lambda)) = \Psi \boldsymbol{u}, \text{ in } \Omega(t), \tag{13}$$

$$(\boldsymbol{\sigma}(\nabla \boldsymbol{u}) - \boldsymbol{\sigma}_a(a_b) + \boldsymbol{\sigma}_c(\lambda)) \cdot \boldsymbol{n} = \boldsymbol{T}(\boldsymbol{\kappa}, \lambda) \text{ on } \Gamma(t), \tag{14}$$

where $\boldsymbol{\sigma}$, $\boldsymbol{\sigma}_a$ and $\boldsymbol{\sigma}_c$ are respectively the stress, the protrusive and the contractile tensors; Ψ is an elastic constant proportional to the strength of the adhesion (Zhao et al., 2017); $\boldsymbol{T}$ is the tension traction on the membrane; $\boldsymbol{n}$ is the outward-pointing unit normal to the surface; λ is a Lagrange multiplier which increases if the domain grows and decreases if it shrinks (Elliott et al., 2012); and $\boldsymbol{\kappa}$ is the mean curvature vector. Eq. (13) and (14) are the general mechanical equations coupled to the biochemical reaction–diffusion system. In fact, the stress tensor can take into account elastic, viscous and plastic phenomena. Thus, the general mechanobiological model is composed of Eqs. (1), (9), (10), (13) and (14).

Let us continue with the terms in Eqs. (13) and (14). The simplest stress tensor follows the Hooke's elasticity law, which is given by (Irgens, 2008): $\boldsymbol{\sigma} = \frac{E}{1+\nu}\left(\boldsymbol{\varepsilon} + \frac{\nu}{1-2\nu}\nabla \cdot \boldsymbol{u}\right)$, where $\boldsymbol{\varepsilon}$ is the linear strain tensor, and E and ν refer to the modulus of elasticity and the Poisson's ratio, respectively (Irgens, 2008). Assuming plane-stress conditions and adopting Voigt notation, Hooke's law can be written in the form

$$\begin{bmatrix}\sigma_{11}\\ \sigma_{22}\\ \sigma_{12}\end{bmatrix} = \frac{E}{1-\nu^2}\begin{bmatrix}1 & \nu & 0\\ \nu & 1 & 0\\ 0 & 0 & \frac{1-\nu}{2}\end{bmatrix}\begin{bmatrix}\varepsilon_{11}\\ \varepsilon_{22}\\ 2\varepsilon_{12}\end{bmatrix}. \tag{15}$$

For the active internal forces, expansion and contraction, we choose: (i) an expansion proportional to a_b and a contraction proportional to λ. The former is a common assumption in computational models where the protrusive force results form the concentration of actin filaments (Alt and Tranquillo, 1995; Stéphanou and Tracqui, 2002; Neilson et al., 2011; Madzvamuse and George, 2013). The latter has been proposed in Neilson et al. (2011) to indirectly model myosin contraction as well as membrane tension, leading to movement of the rear end. The expansion and contraction terms can be written as: $\boldsymbol{\sigma}_a = (E/(1-\nu))a_b\varepsilon_0\boldsymbol{I}$ and $\boldsymbol{\sigma}_c = (E/(1-\nu))\lambda\varepsilon_0\boldsymbol{I}$.

The area-control variable is determined by the Lagrange multiplier $\lambda(t)$ which solves the ordinary differential equation for the area constraint (Neilson et al., 2011):

$$\frac{d\lambda}{dt} = \frac{\beta_1\lambda(A - A_0 + dA/dt)}{A_0(\lambda + \beta_1)} - \beta_2\lambda, \qquad \text{with} \qquad \lambda(0) = \lambda_0. \tag{16}$$

Here, A, A_0 and dA/dt are respectively the area, the initial area, and the rate of change of the area; and β_1 and β_2 are positive parameters.

Finally, the mean curvature vector is given by (Heine, 2004; Barrett et al., 2020):

$$\boldsymbol{\kappa} = -\Delta_\Gamma \boldsymbol{x}, \qquad \text{where } \boldsymbol{x} \in \Gamma(t), \tag{17}$$

and the membrane tension is (Neilson et al., 2011):

$$\boldsymbol{T} = \lambda\delta\boldsymbol{\kappa}, \tag{18}$$

where δ is a factor of proportionality of the rigidity of the membrane.

As can be seen in Eq. (13), inertia has been ignored. This can be done since inertial forces are negligible with respect to internal forces, such as elastic and viscous ones (Lewis and Murray, 1991). This means that motion is stopped after unloading (Lewis and Murray, 1991). In this case, we may consider that after each computation of the biochemical model the system undergoes an elastic deformation. We may also consider that after each deformation the cell rapidly relaxes and no elastic energy is accumulated. This is equivalent to solving Eq. (13) without taking into account the pre-strain given by the previous deformation step. This approach is similar to the work in Zhao et al. (2017).

Thus, for the present example, our model is composed of the following partial differential equations: Eqs. (2), (4), (6), (11) to (14), (16) and (17), that describe the evolution of a_1, a_2, a_3, a_b, $\boldsymbol{u}$, $\boldsymbol{\kappa}$ and λ. The full model is summarised in Table 1.

3. A bulk-surface moving-mesh finite element approach to the mechanobiochemical model in 2-space dimensions

Since we have a system of bulk-surface partial differential equations (BS-PDEs) posed on an evolving domain, we need a robust, accurate and consistent numerical method that can compute approximate solutions of the full model. Several numerical methods have been developed and implemented to solve partial differential equations (PDEs) on evolving domains and surfaces. For example, in Novak et al. (2007), finite volumes were applied in a framework with diffusion in the bulk and on the boundary; in Rätz and Röger (2014), Rätz (2015), a phase-field finite-element approach was implemented to deal with a bulk-surface reaction–diffusion system; in Elliott et al. (2017), a model for the dynamics between membrane receptors and ligands was approximated by the piecewise linear coupled bulk-surface finite element method developed in Elliott and Ranner (2013); in Alhazmi (2019), the finite element approach was also implemented to solve a reaction–diffusion system able to form patterns; and in Frittelli et al. (2021), by combining the virtual element method (Brezzi et al., 2014) and the surface finite element method (Dziuk and Elliott, 2013), the authors delivered a new method to solve BS-PDEs.

In this work, we employ a bulk-surface moving-mesh finite element method (BS-MFEM) to solve bulk and surface PDEs on time-dependent domains and surfaces. We assume that the mesh velocity is different from the material velocity, as presented for the arbitrary Lagrangian–Eulerian formulation in Mackenzie et al. (2021), Dziuk and Elliott (2013) and Elliott and Styles (2012). In the bulk, we will further assume that Eq. (11) is a time-independent system. Given that the coupling is through Dirichlet boundary conditions, we will use the standard bulk finite element formulation. The remaining time-dependent terms will be solved using the Euler finite difference time-stepping scheme. To ensure the regularity of the finite element mesh and the convergence of the BS-MFEM on evolving domains and surfaces, we apply smoothing and re-meshing algorithms as appropriately determined by the regularity of the numerical solutions.

3.1. The weak formulation of the mechanobiochemical model

3.1.1. The weak form of the surface reaction–diffusion system

Let us first multiply Eq. (1) by a test function φ and integrate over $\Gamma(t)$; thus, the problem reads: find $a_k \in H^1(\Gamma(t))$ such that:

$$\int_{\Gamma(t)} \varphi\left(\partial^\bullet a_k + a_k \nabla_{\Gamma(t)} \cdot \mathbf{v} - d_k \Delta_{\Gamma(t)} a_k - f_k(\boldsymbol{a})\right) = 0, \tag{19}$$

Table 1
Mathematical model.

Name	Equation	Domain
Membrane polarisation	$\partial^\bullet a_1 + a_1 \nabla_{\Gamma(t)} \cdot \mathbf{v} - d_1 \Delta_{\Gamma(t)} a_1 = \gamma \left(\dfrac{s_e\left(\frac{a_1^2}{a_2} + k_1\right)}{(s_3 + a_3)(1 + s_1 a_1^2)} - r_1 a_1 \right)$	$\boldsymbol{x}(t) \in \Gamma(t)$
	$\partial^\bullet a_2 + a_2 \nabla_{\Gamma(t)} \cdot \mathbf{v} = \gamma \left(k_2 \hat{a}_1 - r_2 a_2 \right)$	$\boldsymbol{x}(t) \in \Gamma(t)$
	$\partial^\bullet a_3 + a_3 \nabla_{\Gamma(t)} \cdot \mathbf{v} - d_3 \Delta_{\Gamma(t)} a_3 = \gamma \left(k_3 a_1 - r_3 a_3 \right)$	$\boldsymbol{x}(t) \in \Gamma(t)$
	$a_1 = a_{10},\ a_2 = a_{20},\ a_3 = a_{30}$	$\boldsymbol{x}(t) \in \Gamma(0)$
Kinematic model	$\mathbf{v} = \dfrac{d\mathbf{u}}{dt}$	$\boldsymbol{x}(t) \in \Omega(t)$
Cytoplasmic polarisation	$0 = d_b \Delta a_b - C_b a_b + G_b$	$\boldsymbol{x}(t) \in \Omega(t)$
	$a_b = a_3$	$\boldsymbol{x}(t) \in \Gamma(t)$
Mechanical model	$\nabla \cdot (\boldsymbol{\sigma}(\nabla \boldsymbol{u}) - \boldsymbol{\sigma_a}(a_b) + \boldsymbol{\sigma}_c(\lambda)) = \boldsymbol{\Psi u}$	$\boldsymbol{x}(t) \in \Omega(t)$
	$(\boldsymbol{\sigma}(\nabla \boldsymbol{u}) - \boldsymbol{\sigma_a}(a_b) + \boldsymbol{\sigma}_c(\lambda)) \cdot \boldsymbol{n} = \lambda \delta \boldsymbol{\kappa}$	$\boldsymbol{x}(t) \in \Gamma(t)$
	$\boldsymbol{\kappa} = -\Delta_\Gamma \boldsymbol{x}$	$\boldsymbol{x}(t) \in \Gamma(t)$
	$\dfrac{d\lambda}{dt} = \dfrac{\beta_1 \lambda (A - A_0 + dA/dt)}{A_0(\lambda + \beta_1)} - \beta_2 \lambda$	$t \in [0, T_f]$

for all $\varphi \in H^1(\Gamma(t))$. The divergence theorem for closed surfaces is given by Dziuk and Elliott (2007):

$$\int_\Gamma \nabla_\Gamma \xi \cdot \nabla_\Gamma \eta = -\int_\Gamma \xi \Delta_\Gamma \eta, \tag{20}$$

where $\xi(\boldsymbol{x}), \eta(\boldsymbol{x}) : \Gamma \to \mathbb{R}$. Notice that due to the absence of boundary, there is no flux term. Eq. (19) can be therefore rewritten as:

$$\int_{\Gamma(t)} \varphi \left(\partial^\bullet a_k + a_k \nabla_{\Gamma(t)} \cdot \mathbf{v} - f_k(\boldsymbol{a}) \right) + \int_{\Gamma(t)} \nabla_{\Gamma(t)} \varphi \cdot d_k \nabla_{\Gamma(t)} a_k = 0 \qquad \forall \varphi \in H^1(\Gamma(t)). \tag{21}$$

We can rewrite the first two terms of the left-hand side in the following way:

$$\int_{\Gamma(t)} \varphi \left(\partial^\bullet a_k + a_k \nabla_{\Gamma(t)} \cdot \mathbf{v} \right) = \int_{\Gamma(t)} \left(\partial^\bullet (\varphi a_k) - a_k \partial^\bullet \varphi + \varphi a_k \nabla_{\Gamma(t)} \cdot \mathbf{v} \right) \qquad \forall \varphi \in H^1(\Gamma(t)).$$

Then, applying the Reynolds transport theorem (Acheson, 1990; Marsden and Chorin, 1993; Madzvamuse, 2000; Dziuk and Elliott, 2007, 2013), the weak form reads: find $a_k \in H^1(\Gamma(t))$ such that:

$$\frac{d}{dt} \int_{\Gamma(t)} \varphi a_k - \int_{\Gamma(t)} a_k \partial^\bullet \varphi + \int_{\Gamma(t)} \nabla_{\Gamma(t)} \varphi d_k \cdot \nabla_{\Gamma(t)} a_k = \int_{\Gamma(t)} \varphi f_k(\boldsymbol{a}), \tag{22}$$

for all $\varphi \in H^1(\Gamma(t))$. Since $\varphi \in H^1(\Gamma(t))$, its material derivative is also given by: $\partial^\bullet \varphi = \frac{\partial \varphi}{\partial t} + \mathbf{v} \cdot \nabla \varphi$.

3.1.2. The weak form of the curvature equation

Let us first define the scalar product of two second order tensors of dimension n as: $\alpha = \boldsymbol{A} : \boldsymbol{B} := \sum_{i=1}^{i=n} \sum_{j=1}^{j=n} A_{ij} B_{ij}$. Multiplying Eq. (17) by a test function $\boldsymbol{\varphi}$ and integrating over $\Gamma(t)$ yields:

$$\int_{\Gamma(t)} \boldsymbol{\varphi} \cdot \boldsymbol{\kappa} = -\int_{\Gamma(t)} \boldsymbol{\varphi} \Delta_{\Gamma(t)} \boldsymbol{x}. \tag{23}$$

Then, following Eq. (20), the weak problem reads: find $\boldsymbol{\kappa} \in H^1(\Gamma(t)) \times H^1(\Gamma(t))$ such that:

$$\int_{\Gamma(t)} \boldsymbol{\varphi} \cdot \boldsymbol{\kappa} = \int_{\Gamma(t)} \nabla_{\Gamma(t)} \boldsymbol{\varphi} : \nabla_{\Gamma(t)} \boldsymbol{x}, \qquad \forall \boldsymbol{\varphi} \in H^1(\Gamma(t)) \times H^1(\Gamma(t)). \tag{24}$$

3.1.3. The weak form of the bulk reaction–diffusion system

Multiplying Eq. (11) by a test function φ, integrating it over $\Gamma(t)$ and applying Green's theorem yields the weak problem: find $a_b \in H^1(\Omega(t))$ such that:

$$\int_{\Gamma(t)} \varphi d_b \nabla a_b \cdot \boldsymbol{n} + \int_{\Omega(t)} \left(-\nabla \varphi \cdot d_b \nabla a_b - \varphi C_b a_b + \varphi G_b \right) = 0, \tag{25}$$

for all $\varphi \in H^1(\Omega(t))$. Further, since from Eq. (10) a_b is known at the boundary, $\varphi \in H_0^1(\Omega(t)) = \left\{ \varphi \in H^1(\Omega(t)) : \varphi|_{\Gamma(t)} = 0 \right\}$. Hence, the weak problem reads: find $a_b \in H^1(\Omega(t))$ such that:

$$\int_{\Omega(t)} \left(-\nabla \varphi \cdot d_b \nabla a_b - \varphi C_b a_b + \varphi G_b \right) = 0, \tag{26}$$

for all $\varphi \in H_0^1(\Omega(t))$.

3.1.4. The weak form of the mechanical model

The weak form for Eq. (14) reads: find $\boldsymbol{u} \in H^1(\Omega(t)) \times H^1(\Omega(t))$ such that:

$$\int_{\Gamma(t)} \boldsymbol{\varphi} \cdot \boldsymbol{T} + \int_{\Omega(t)} \left(-\nabla \boldsymbol{\varphi} : \left(\boldsymbol{\sigma} - \boldsymbol{\sigma_a} + \boldsymbol{\sigma}_c \right) - \boldsymbol{\varphi} \cdot \boldsymbol{\Psi u} \right) = 0, \tag{27}$$

for all $\boldsymbol{\varphi} \in H^1(\Omega(t)) \times H^1(\Omega(t))$.

3.2. Space-discretisation

3.2.1. The finite element approximation of the surface reaction–diffusion system

Let us first approximate $\Gamma(t)$ by a polygonal curve $\Gamma^h(t) \subset \mathcal{U}(t)$ with a set of vertices $\mathcal{N}^h(t) = \left\{ \boldsymbol{X}_j(t) \right\}_{j=1}^N \in \Gamma(t)$ and a set of segments $\mathcal{T}^h(t) = \left\{ \mathcal{T}_e^h(t) \right\}_{e=1}^N$. Note that since the curve is closed, the number of vertices is equal to the number of segments. We now define a finite element space for each $\Gamma^h(t)$ as (Dziuk and Elliott, 2007): $S^h(\Gamma^h(t)) = \left\{ \varphi^h \in C^0(\Gamma^h(t)) : \varphi^h|_{\mathcal{T}_e^h} \text{ is linear affine for each } \mathcal{T}_e^h(t) \in \mathcal{T}^h(t) \right\}$, with basis functions $\left\{ \chi_j \right\}_{j=1}^N$.

We now write the finite element problem as: find $a_k^h(t) \in S^h(\Gamma^h(t))$ such that

$$\frac{d}{dt} \int_{\Gamma(t)} \varphi a_k^h - \int_{\Gamma^h(t)} a_k^h \partial^\bullet \varphi^h + \int_{\Gamma^h(t)} \nabla_{\Gamma^h(t)} \varphi^h d_k \cdot \nabla_{\Gamma^h(t)} a_k^h = \int_{\Gamma^h(t)} \varphi^h f_k(\boldsymbol{a}^h), \tag{28}$$

for all $\varphi^h \in S^h(\Gamma^h(t))$.

As shown in Elliott and Styles (2012) and Dziuk and Elliott (2013), the discrete basis functions have the following transport property when the mesh velocity is different from the material velocity:

$$\partial^\bullet \chi_j = (\mathbf{v}^h - \mathbf{v}_M^h) \cdot \nabla_{\Gamma^h(t)} \chi_j, \tag{29}$$

where $\mathbf{v}^h$ is the interpolated material velocity on $\Gamma^h(t) \ni \boldsymbol{x}$, $\mathbf{v}^h(\boldsymbol{x}, t) = \sum_{j=1}^N \mathbf{v}(\boldsymbol{X}_j(t), t) \chi_j(\boldsymbol{x}, t)$, and $\mathbf{v}_M^h$ is the mesh velocity: $\mathbf{v}_M^h(\boldsymbol{x}, t) = \sum_{j=1}^N \dot{\boldsymbol{X}}_j(t) \chi_j(\boldsymbol{x}, t)$.

Let us write $a_k^h(\boldsymbol{x},t) \in S^h(\Gamma^h(t))$ as $a_k^h(\boldsymbol{x},t) = \sum_{j=1}^N \chi_j(\boldsymbol{x})(A_k(t))_j$, where $A_k(t) \in \mathbb{R}^N$ is the vector of approximated nodal values of a_k^h at time t, and $(A_k(t))_j$ are the nodal values. Applying the transport property, Eq. (29), we have the following system of ordinary differential equations:

$$\frac{d}{dt}\int_{\Gamma^h(t)} \chi_i\chi_j(A_k)_j + \int_{\Gamma^h(t)} \nabla_{\Gamma^h(t)}\chi_i d_k \cdot \nabla_{\Gamma^h(t)}\chi_j(A_k)_j = \int_{\Gamma^h(t)} \chi_i f_k(\boldsymbol{a}^h) + \int_{\Gamma^h(t)} (\mathbf{v}^h - \mathbf{v}_M^h)\cdot\nabla_{\Gamma^h(t)}\chi_i\chi_j(A_k)_j. \tag{30}$$

This is an extended version of the evolving surface finite element method (ESFEM) where the mesh velocity differs from the material velocity which has been referred to as the Arbitrary Lagrangian–Eulerian ESFEM (ALE-ESFEM) (Elliott and Styles, 2012; Dziuk and Elliott, 2013; Mackenzie et al., 2021). In the case that the mesh and material velocities are identical, the discrete material velocity vanishes; hence, so does the second term at the right-hand-side of Eq. (30). It seems convenient to let the mesh velocity be equal to the material velocity; yet, this can rapidly lead to poor mesh quality as the domain deforms (Elliott and Styles, 2012). Therefore, we will consider a different mesh velocity to reduce mesh distortion along simulations. As will be shown below, such a velocity $\mathbf{v}_M^h$ will be given by mesh smoothing.

3.2.2. The finite element approximation of the curvature equation

We employ the same set of vertices $\mathcal{N}^h(t) = \{\boldsymbol{X}_j(t)\}_{j=1}^N$ as outlined in the previous section. However, the regularity of the solutions requires us to employ at least a quadratic finite element space (Heine, 2004). Therefore, we will approximate $\Gamma(t)$ by a piecewise quadratic curve $\Gamma^q(t)$ – here, we used the superscripts $(\cdot)^q$ to differentiate this approximation from Γ^h – described by $\mathcal{N}^h(t)$ and a set of quadratic segments $\mathcal{T}^q(t) = \{\mathcal{T}_e^q\}_{e=1}^{N/2}$. The finite element space is then: $Q^q(\Gamma^q(t)) = \left\{\varphi^q \in C^0(\Gamma^q(t)) : \varphi^q|_{\mathcal{T}_e^q} \text{ is quadratic for each } \mathcal{T}_e^q(t) \in \mathcal{T}^q(t)\right\}$, and the finite element problem reads: find $\boldsymbol{\kappa}^q \in Q^q(\Gamma^q(t))\times Q^q(\Gamma^q(t))$ such that:

$$\int_{\Gamma^q(t)} \boldsymbol{\varphi}^q\cdot\boldsymbol{\kappa}^q = \int_{\Gamma^q(t)} \nabla_{\Gamma^q(t)}\boldsymbol{\varphi}^q : \nabla_{\Gamma^q(t)}\boldsymbol{x}^q, \tag{31}$$

$\forall \boldsymbol{\varphi}^q \in Q^q(\Gamma^q(t))\times Q^q(\Gamma^q(t))$.

3.2.3. The finite element approximation of the bulk reaction–diffusion system

Let us now generate the bulk triangulation $\Omega^h(t)$ of $\Omega(t)$ and its corresponding finite element space. We will consider a set of nodes $\mathcal{N}^h(t) = \{\boldsymbol{X}_j(t)\}_{j=1}^{N_b} \in \Omega(t)$ and a set of triangles $\mathcal{T}^h(t) = \{\mathcal{T}_e^h(t)\}_{e=1}^{N_T}$ such that $\partial\Omega^h(t) = \Gamma^h(t)$. The finite element space will be defined as: $V^h(\Omega^h(t)) = \left\{\varphi^h \in C^0(\Omega^h(t)) : \varphi^h|_{\mathcal{T}_e^h} \text{ is linear affine for each } \mathcal{T}_e^h(t) \in \mathcal{T}^h(t)\right\}$. Thus, the finite element problem reads: find $a_b^h \in V^h(\Omega^h(t))$ such that:

$$\int_{\Omega^h(t)} \left(\nabla\varphi^h\cdot d_b\nabla a_b^h + \varphi C_b a_b^h - \varphi G_b\right) = 0, \tag{32}$$

for all $\varphi^h \in V_0^h(\Omega^h(t))$, where $V_0^h(\Omega^h(t)) = \{\varphi^h \in V^h(\Omega^h(t)) : \varphi^h|_{\Gamma^h(t)} = 0\}$.

3.2.4. The finite element approximation of the mechanical model

We use the same triangulation and the same finite element space as in the previous section to formulate the finite element method for the mechanical model. Hence, the problem reads: find $\boldsymbol{u}^h \in V^h(\Omega^h(t))\times V^h(\Omega^h(t))$ such that:

$$\int_{\Gamma^h(t)} \boldsymbol{\varphi}^h\cdot\boldsymbol{T}^h + \int_{\Omega^h(t)} \left(-\nabla\boldsymbol{\varphi}^h : \left(\boldsymbol{\sigma}^h - \boldsymbol{\sigma}_a^h + \boldsymbol{\sigma}_c^h\right) - \boldsymbol{\varphi}^h\cdot\Psi\boldsymbol{u}^h\right) = 0, \tag{33}$$

for all $\boldsymbol{\varphi}^h \in V^h(\Omega^h(t))\times V^h(\Omega^h(t))$.

3.3. Time-discretisation of the mechanobiochemical model

3.3.1. The time-discretisation of the spatially discretised surface reaction–diffusion system

To solve the system of surface reaction–diffusion equations on an evolving surface, we still need to discretise the time-domain of Eq. (30). Thus, we will look for approximations of $A_k(t)$ that can be defined as $A_k(\tau m) \approx A_k^m$, where τ is the time-step and $m \in \mathbb{N}$. Applying a Backward-Euler time-integration scheme, we have: find $A_k^{m+1} \in \mathbb{R}^N$ such that:

$$\frac{1}{\tau}\left(\int_{\Gamma^{m+1}} \chi_i^{m+1}\chi_j^{m+1}(A_k^{m+1})_j - \int_{\Gamma^m} \chi_i^m\chi_j^m(A_k^m)_j\right) + \int_{\Gamma^{m+1}} \nabla_{\Gamma^{m+1}}\chi_i^{m+1}\cdot d_k\nabla_{\Gamma^{m+1}}\chi_j^{m+1}(A_k^{m+1})_j = \int_{\Gamma^{m+1}} \chi_i^{m+1} f_k((\boldsymbol{a}^h)^{m+1}) + \int_{\Gamma^{m+1}} (\mathbf{v}^h - \mathbf{v}_M^h)^{m+1}\cdot\nabla_{\Gamma^{m+1}}\chi_i^{m+1}\chi_j^{m+1}(A_k^{m+1})_j. \tag{34}$$

Eq. (34) in matrix–vector form is postulated as:

$$\frac{1}{\tau}\left(\mathcal{M}^{m+1}{A_k}^{m+1} - \mathcal{M}^m{A_k}^m\right) + d_k\mathcal{S}^{m+1}A_k^{m+1} = {\mathcal{F}_k}^{m+1} + \mathcal{T}^{m+1}A_k^{m+1}, \tag{35}$$

where

$$\mathcal{M}^m = \int_{\Gamma^m} \chi_i^m\chi_j^m, \qquad \mathcal{S}^m = \int_{\Gamma^m} \nabla_{\Gamma^m}\chi_i^m\cdot\nabla_{\Gamma^m}\chi_j^{m+1},$$
$$\mathcal{F}_k^m = \int_{\Gamma^m} \chi_i^m f_k((\boldsymbol{a}^h)^m), \qquad \mathcal{T}^m = \int_{\Gamma^m} (\mathbf{v}^h - \mathbf{v}_M^h)^m\cdot\nabla_{\Gamma^m}\chi_i^m\chi_j^m.$$

Notice that $\mathcal{F}_k$ is nonlinear due to f_k.

In addition, in Eq. (6), a_2 is homogeneous along $\Gamma(t)$ for all $t \in [0,T_f]$. Therefore, the diffusion term of Eq. (34) is zero and the equation for a_2 simplifies as: find $A_2^{m+1} \in \mathbb{R}^N$ such that

$$\frac{1}{\tau}\left(\mathcal{M}^{m+1}{A_2}^{m+1} - \mathcal{M}^m{A_2}^m\right) = {\mathcal{F}_2}^{m+1} + \mathcal{T}^{m+1}A_2^{m+1}. \tag{36}$$

To numerically deal with the nonlinearities in Eq. (34), which are due to the f_k, we employ the Newton–Raphson scheme. Since, we are using the user-defined element subroutine (UEL) of ABAQUS, we need to define the residual (Eq. (38)) and the tangent (Eq. (39)) equations. Thus, the numerical algorithm reads: find $A_k^{m+1} = \left(A_k^{m+1}\right)_{r+1}$ such that $\left(A_k^{m+1}\right)_{r+1} - \left(A_k^{m+1}\right)_r \le 10^{-6}$ with:

$$\frac{\partial R_k^{m+1}}{\partial A_l^{m+1}}\left(\left(A_k^{m+1}\right)_{r+1} - \left(A_k^{m+1}\right)_r\right) = -R_k^{m+1}, \tag{37}$$

where $(A_k^{m+1})_0 = A_k^m$. The residual equation is stated as follows:

$$R_k^{m+1} = \frac{1}{\tau}\left(\mathcal{M}^{m+1}{A_k}^{m+1} - \mathcal{M}^m{A_k}^m\right) + d_k\mathcal{S}^{m+1}A_k^{m+1} - {\mathcal{F}_k}^{m+1} - \mathcal{T}^{m+1}A_k^{m+1}, \tag{38}$$

while the tangent equation states:

$$\frac{\partial R_k^{m+1}}{\partial A_l^{m+1}} = \begin{cases} \frac{1}{\tau}\mathcal{M}^{m+1} + d_k\mathcal{S}^{m+1} - \mathcal{T}^{m+1} - \frac{\partial\mathcal{F}_k^{m+1}}{\partial {A_l}^{m+1}} & \text{for } k = l, \\ -\frac{\partial\mathcal{F}_k^{m+1}}{\partial {A_l}^{m+1}} & \text{for } k \ne l, \end{cases} \tag{39}$$

where:

$$\frac{\partial\mathcal{F}_k^{m+1}}{\partial {A_l}^{m+1}} = \int_{\Gamma^{m+1}} \varphi^{m+1}\varphi^{m+1}\frac{\partial f_k}{\partial a_l}(\boldsymbol{a}^{m+1}).$$

3.3.2. The approximation of the Lagrange multiplier or area constraint $\lambda(t)$

To proceed, we now need to solve Eq. 16 for the Lagrange multiplier or area constraint $\lambda(t)$. Here, we employ the simple forward Euler scheme, thus:

$$\frac{d\lambda}{dt} \approx \frac{\lambda^{m+1} - \lambda^m}{\tau} = \frac{\beta_1 \lambda (A^m - A_0 + (\Delta A/\tau)^m)}{A_0(\lambda^m + \beta_1)} - \beta\lambda^m. \tag{40}$$

The terms $(\Delta A/\tau)^m$ and A^m are, respectively, the change of area and the area at time τm. Therefore, $(\Delta A)^m = A^m - A^{m-1}$.

3.4. Mesh smoothing and adaptive re-meshing algorithms

Two mesh smoothing algorithms are used to improve the quality of the finite element triangulation throughout the simulation. First, a surface mesh equidistribution scheme is implemented by means of the De Boor's algorithm (de Boor, 1973) and the parametric quadratic mesh. Second, the Durand et al.'s (2019) algorithm is implemented to smooth the bulk mesh. Notice that the surface mesh is made up of nodes present in the bulk mesh. Additionally, as the cell deforms continuously in space and time, a re-meshing scheme is also utilised in cases where the mesh quality drops bellow a specific threshold, monitoring, a posteriori, the mesh regularity during evolution. This re-meshing scheme is based on the Mesh2D toolbox (Engwirda, 2005, 2014).

First, let us describe the mesh smoothing algorithm used on the surface. Since we defined a quadratic finite element mesh for the surface, we use the quadratic parameterisation to equidistribute the mesh. To do this, we need to define a transformation from $\boldsymbol{x} \in \Gamma^q \subset \mathbb{R}^2$ to $x \in [0, L] \subset \mathbb{R}$, with L the perimeter of Γ^q, such that the size of each element on Γ^q is equal to the size of the image element in $[0, L]$. We might use a local transformation for $\xi \in [-1, 1]$ for each element for easy computations of the arc length. Then, we use the De Boor's algorithm to reorganise the nodes, such that the distance between each pair of adjacent nodes is equal. After that, we use the inverse transformation to reconstruct the curve. We might use several iterations to improve the equidistribution.

Let us start by defining the local transformation and the element arc length. Let $\boldsymbol{x}_1^e$, $\boldsymbol{x}_2^e$ and $\boldsymbol{x}_3^e$ be, respectively, the start-, the end- and the middle-nodes of an element $\mathcal{T}_e^q$. The transformation is then:

$$\boldsymbol{x}^e(\xi) = [x^e, y^e]^\top = \theta_1^e(\xi)\boldsymbol{x}_1^e + \theta_2^e(\xi)\boldsymbol{x}_2^e + \theta_3^e(\xi)\boldsymbol{x}_3^e, \tag{41}$$

where θ_i^e are defined as: $\theta_1^e = 0.5\xi(\xi - 1)$, $\theta_2^e = 0.5\xi(\xi + 1)$, $\theta_3^e = 1 - \xi^2$. The arc length of each element $\mathfrak{A}_l^e$ can be computed as the arc length of the parametric curve defined in Eq. (41):

$$\begin{aligned}\mathfrak{A}_l^e &= \int_{-1}^{1} \sqrt{\left(\left(\frac{dx^e}{d\xi}\right)^2 + \left(\frac{dy^e}{d\xi}\right)^2\right)} \\ &= \int_{-1}^{1} \sqrt{\left(\sum_{i=1}^{3} \frac{d\theta_i^e}{d\xi} x_i^e\right)^2 + \left(\sum_{i=1}^{3} \frac{d\theta_i^e}{d\xi} y_i^e\right)^2}\, d\xi,\end{aligned} \tag{42}$$

which can be approximated by Gaussian quadrature. Next, the total arc length is computed by $\mathfrak{A}_L = \sum_{e=1}^{(N/2)} \mathfrak{A}_l^e$. Since we want to equidistribute the surface mesh, each element must have $\mathfrak{A}_L/(N/2)$ arc length and using the De Boor's algorithm we find the appropriate node locations.

Let $\mathfrak{A}_L^{z_e}$ be the arc length from the first node until the end of element e, e.g. if $e = 3$, $\mathfrak{A}_L^{z_3} = \mathfrak{A}_l^1 + \mathfrak{A}_l^2 + \mathfrak{A}_l^3$. Since each element must have arc length $\mathfrak{A}_L/(N/2)$, we need to find a new $\boldsymbol{x}_2^e$, say $\hat{\boldsymbol{x}}_2^e$, such that the new arc length is $\hat{A}_L^{z_e} = e\mathfrak{A}_L/(N/2)$. Thus, by De Boor's algorithm we need to find an element r such that: $\mathfrak{A}_L^{z_{r-1}} \leq (e\mathfrak{A}_L/(N/2)) \leq \mathfrak{A}_L^{z_r}$. This means that $\hat{\boldsymbol{x}}_2^e$ belongs to element r. Then, we find: $\hat{\boldsymbol{x}}_2^e$ such that:

$$\frac{e\mathfrak{A}_L}{N/2} - \mathfrak{A}_L^{z_{r-1}} = \int_{-1}^{\xi(\hat{\boldsymbol{x}}_2^e)} \sqrt{\left(\sum_{i=1}^{3} \frac{d\theta_i^r}{d\xi} x_i^r\right)^2 + \left(\sum_{i=1}^{3} \frac{d\theta_i^r}{d\xi} y_i^r\right)^2}\, d\xi. \tag{43}$$

Again, we use Gaussian quadrature to approximate $\xi(\hat{\boldsymbol{x}}_2^e)$, although we need to iterate several times. Once we have $\xi(\hat{\boldsymbol{x}}_2^e)$, we use Eq. (41) on element r to find $\hat{\boldsymbol{x}}_2^e$.

Using this procedure, we set an equidistant mesh. However, since we are working on a closed curve, there are infinite possible meshes. For the purpose of uniqueness, we add an additional constraint such that the distance between the initial mesh and the final mesh is minimal. Let us first recall the initial mesh on $[0, L]$ with the set of points $\{x_j\}_{j=1}^N$ and the target set of points $\{y_j\}_{j=1}^N$. We then establish the optimisation problem as: find $\{y_j\}_{j=1}^N$ such that:

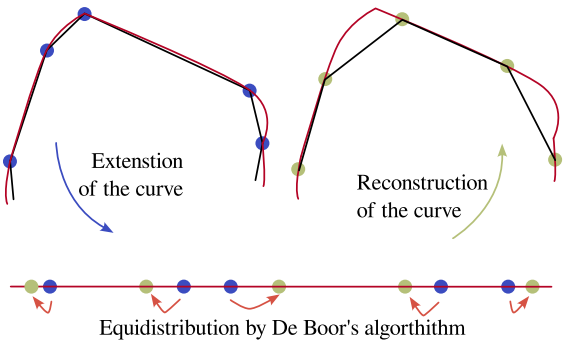

Fig. 3. Surface smoothing scheme. The De Boor's algorithm is used to equidistribute curved meshes. The illustration indicates how the nodes are relocated along the length of the discrete contour.

$$y_j - y_{j-1} = \Delta y \text{ is constant} \tag{44}$$

and

$$\left(\sum_{j=0}^{N} (x_j - y_j)^2\right)^{1/2} \text{ is minimal.} \tag{45}$$

By De Boor's algorithm we satisfy Eq. (44) and, acknowledging that defining y_0 we only find one equidistant mesh, we set the target function as:

$$F(y_0) = \left(\sum_{j=0}^{N} (x_j - (y_0 + j\Delta y))^2\right)^{1/2}. \tag{46}$$

This attains its minimum value when

$$y_0 = \frac{\left(\sum_{j=0}^{N} x_j\right) - \left(\frac{\Delta y N(N+1)}{2}\right)}{N}, \tag{47}$$

which can be negative since Γ^q is a closed curve. Thus, the algorithm for equidistribution on the curve with minimal mesh displacement is as follows: (i) set a mapping from Γ^q to $[0, L]$, (ii) define $\Delta y = L/N$, (iii) establish y_0 with Eq. (47), (iv) use De Boor's algorithm to compute the other nodes, and (v) apply the inverse mapping with the Gaussian quadrature to solve Eq. (43). A schematic representation is shown in Fig. 3.

Now, for the bulk mesh smoothing we use the method introduced in Durand et al. (2019). We also adopt their mesh quality metric, which for a triangle element is given by Durand et al. (2019):

$$\mathcal{Q}_T = \left(\frac{6\sqrt{\frac{A_T}{\sqrt{3}}}}{p_T}\right)^2. \tag{48}$$

In the case that this method fails in improving the minimum quality, $\mathcal{Q}_{\min}$, above some threshold, say $\mathcal{Q}^*_{\min}$, we use the Mesh2D toolbox (Engwirda, 2005, 2014) to re-mesh the domain. Since the bulk variables are not time-dependent, it is not necessary to map the variables after the re-meshing scheme. Additionally, the equidistant surface mesh is provided as an input to Mesh2D and remains unmodified. Therefore, the surface variables do not need to be mapped either.

The full algorithm can be summarised as follows:

1. Set the initial mesh
   (a) Generate an initial piecewise linear mesh on the surface with a even number of nodes.

(b) Use the Engwirda's (2005, 2014) toolbox Mesh 2D to create a piecewise linear triangular mesh.
(c) Create a quadratic set of surface elements using the same nodes of Item 1a.
(d) Use the Durand et al.'s (2019) algorithm to smooth the mesh.

2. Solution of field variables at time $n\tau$.

(a) Approximate a_1 and a_3 through Eq. (38).
(b) Approximate a_2 through Eq. (36).
(c) Approximate $\boldsymbol{\kappa}$, a_b and $\boldsymbol{u}$ through Eqs. (31)–(33).
(d) Update the nodal positions as $\boldsymbol{x}^{n+1} = \boldsymbol{x}^n + \boldsymbol{u}^n$.
(e) Approximate λ through Eq. (40).
(f) If $n\tau = T_f$ go to Item 4.

3. Improve mesh quality

(a) Use the de Boor's (1973) algorithm to equidistribute the surface mesh.
(b) Use the Durand et al.'s (2019) to smooth the solid mesh until the mesh change by L_2-norm is less than Ite_{tol} or the maximum number of iterations Ite_{max} is reached. If $\mathcal{Q}_{\text{min}} > \mathcal{Q}^*_{\text{min}}$ go to Item 2 if not go to Item 1.

4. Finish.

4. Validation of the bulk-surface finite element method

4.1. Numerical validation of the bulk-surface moving-mesh finite element approach

Next, we will test the convergence of the bulk-surface moving-mesh finite element approach. For that, we will run a simulation of a cell undergoing chemotaxis, where the domain centroid moves from $(0, 0)$ to $(0, 0.5)$ with several time-steps and different numbers of boundary nodes. We will compute the L_2-norm of the displacement error considering the simulation with the smallest time step and the largest number of boundary nodes as the gold standard. For the L_2-norm, we will map the displacement field of each simulation onto the initial mesh of the gold standard. This will allow us to compute the displacement error as: $\sqrt{\int_{\Omega_0}(\boldsymbol{u}_r - \boldsymbol{u})\cdot(\boldsymbol{u}_r - \boldsymbol{u})d\Omega_0}$.

We then proceed to investigate the response of Meinhardt's model on a stationary two-dimensional closed hypersurface. The idea here is to test the response with several combinations of parameters in terms of signal amplification and adaptation to new signals.

We exhibit results of the whole computational algorithm under two different combinations of parameters. One of them corresponding to chemotactic migration and the other to spontaneous movement. These numerical tests are computed using the numerical methods presented in the previous section in a desktop computer with a quad-core processor with 2.40 GHz of base frequency and 32 Gb of RAM.

Table 2 shows the displacement errors for a simulation time of $T_f = 4.0$, which was the common time at which no simulation required remeshing. As can be seen, the displacement error reduces as the time-step becomes smaller and the number of nodes larger. From these results, we will take $\tau = 0.001$ and 2000 nodes to define the initial contour.

4.2. Meinhardt's model for cell polarisation

Let us fix a_{10}, a_{20}, a_{30} γ, k_1, k_2, s_3, r_1, r_2, r_3, η_s and η_n (see Table 3) using the values from Meinhardt (1999), Neilson et al. (2011) and Elliott et al. (2012). We shall vary k_3 and s_1 – as their values differ slightly among (Meinhardt, 1999; Neilson et al., 2011; Elliott et al., 2012) – as well as d_1 and d_3 to identify appropriate parameters for chemotactic and spontaneous migration.

Table 2
Convergence of the displacement field varying N, the number of boundary nodes and τ, the time step. The L_2-norm of the displacement error is computed assuming as reference displacement the result of the simulation with $N = 4000$ and $\tau = 0.0001$.

N	$\tau = 0.002$	$\tau = 0.0005$	$\tau = 0.0002$	$\tau = 0.0001$
1000	1.334e−02	1.305e−02	1.303e−02	1.299e−02
2000	1.274e−02	1.053e−02	1.012e−02	9.945e−03
4000	3.653e−03	1.279e−03	6.734e−04	0.000e+00

Table 3
Fixed parameters for Meinhardt's model for cell polarisation. γ was taken from (Elliott et al., 2012), and the * indicates the values taken from (Meinhardt, 1999).

$\gamma^\star\star$	$k_1^\star$	$k_2^\star$	$s_3^\star$	$r_1^\star$	$r_2^\star$	$r_3^\star$	$\eta_s^\star$	$\eta_n^\star$	a_{10}	a_{20}	a_{30}
2500	0.1	0.03	0.2	0.02	0.03	0.013	0.02	0.01	1.0	1.0	1.0

Table 4
Meinhardt's model response. Summary of the response of Meinhardt's model for cell polarisation with different parameters.

Experiment	k_3	s_1	d_1	d_3	N_p	w	$a_1^{\max}$	Adaptation
1	0.005	0.005	10	100	1	2.127	7.72	Yes
2	0.005	0.005	10	60	1	2.218	6.91	Yes
3	0.005	0.005	10	50	1	2.259	6.6	Yes
4	0.005	0.01	10	30	1	2.717	4.78	Yes
5	0.005	0.005	10	30	1	2.441	5.69	Yes
6	0.005	0.0025	10	30	1	2.262	6.48	Yes
7	0.0025	0.005	10	30	1	2.975	8.1	Yes
8	0.005	0.01	10	20	1	3.135	4.15	Yes
9	0.005	0.005	10	20	1	2.677	4.94	Yes
10	0.005	0.0025	10	20	1	2.466	5.58	Yes
11	0.0025	0.005	10	20	1	3.299	7.18	Yes
12	0.005	0.01	10	15	1	3.415	3.68	Yes
13	0.005	0.005	10	15	1	2.934	4.4	Yes
14	0.005	0.0025	10	15	1	2.680	4.96	Yes
15	0.0025	0.005	10	15	1	3.654	6.49	Yes
16	0.005	0.005	1	2.5	2	1.949	6.46	No
17	0.005	0.005	1	2	2	2.079	5.94	No

For this experiment, the domain is a circle of radius 1 centred at $(0, 0)$, the finite element discretisation is composed of 2000 nodes and elements and the time-step is 0.001. The signal is set at $(5, 5)$ from time 0 to 15 and at $(-5, -5)$ from 15 to the end of the simulation. We then consider the following measures: the number of peaks N_p which are associated to the leading edges, the highest value of the activator $a_1^{\max}$, the width w of the peaks above $a_1^{\max}/2$ and whether the model is able to adapt to a new signal. N_p allows us to determine the ability of the model to yield a polarised state, $a_1^{\max}$ indicates the strength of the polarisation and w defines how localised it is. In addition, $N_p > 1$ indicates the presence of competing leading edges.

4.3. Chemotactic-driven directed cell migration

For the solution of the complete model, let us set the parameters of the mechanical model as presented in Table 5. These parameters were selected in order to validate the general ability of the computational framework to reproduce key features and properties observed during single cell migration and are not experimentally determined. A more rigorous selection would require: (i) the selection of a specific type of cell, (ii) the substratum attachment strength to define Ψ, (iii) its elastic properties ν and E, the calibration of β_1 and β_2 to set the response speed of the area control mechanism through the Lagrange multiplier λ, (iv) the membrane tension to properly define δ, and (v) the relation between the formation of actin filaments and the mechanical stress induced to set ϵ_0. We defer such an experiment for future studies where we will also try and recover some of these parameters through inverse approaches for parameter estimation, using Bayesian methods (Campillo-Funollet et al., 2019).

For chemotactic cell migration, we choose the parameters for Exp. 11 (in Table 4) as explained in the next section. The initial cell domain

Table 5
Parameters of the mechanical model. The last three parameters, namely $\mathcal{Q}^*_{\min}$, $Ite_{\max}$ and Ite_{tol}, are parameters of the mesh smoothing algorithm presented.

Ψ	ν	E	δ	β_1	β_2	λ_0	ϵ_0	$\mathcal{Q}^*_{\min}$	$Ite_{\max}$	Ite_{tol}
0.1	0.45	1	0.001	0.2	0.001	2.0	2.5e−5	0.55	10	0.001

is bounded by a circle of radius 1 centred at $(0,0)$. Furthermore, the system is tested under an initial signalling point at $(5,5)$ that is then changed at $t = 75$ to $(0,10)$. For this simulation, the time-step $\tau = 0.001$, the surface was discretised with 2000 equidistant nodes and the size of the bulk mesh was constraint to 0.25.

4.4. Spontaneous cell migration

In this case, the mechanical model is implemented with the same parameters as presented in Table 5. The initial cell domain is also bounded by a circle of radius 1 centred at $(0,0)$ and for Meinhardt model we use the parameters corresponding to the Exp. 17—again, this choice is explained in the next section. We expect to see unsteady and completely spontaneous cell migration using these parameters and letting $\eta_s = 0$ and $\eta_n = 0$. The initial mesh and the time-step are the same as in the chemotactic-driven directed cell migration case.

5. Exhibiting single cell migration pathways using the bulk-surface moving-mesh finite element method

5.1. Meinhardt's model for cell polarisation

Table 4 shows the results of our experiments. We see that Exp. 16 and Exp. 17, where $d_1 = 1$ and $d_3 = 2$ and 2.5 respectively, had a very different response compared to the others. The system developed two coexisting and competing peaks and was unable to adapt to the signal direction. Additionally, the two coexisting peaks spontaneously changed position. In contrast, in Exp. 1 to Exp. 15, the system developed a single stable peak aligned with the signalling direction that was able to reorient once the signalling direction changed.

Further, in Exp. 1 to Exp. 15, where $d_1 = 10$ and d_3 varied from 15 to 100, it was observed that increasing d_3 made $a_1^{\max}$ larger. However, w decreased, and the system was slower to move from one polarised state to another. This can be explained by the fact that more rapid diffusion of a_3 leads to a non-concentrated distribution, causing its inhibition to have a more global effect. As a result, a_1 can grow more rapidly at regions of maximum values, while is more rapidly inhibited at regions of lower values. Furthermore, decreasing the value of s_1, also increased $a_1^{\max}$ and decreased w. This can also be explained by the fact that reducing s_1 increases the production of a_1 which by definition is enhanced at regions of high values—it is proportional to the square of a_1.

A reduction in k_3 from 0.005 to 0.0025 resulted in higher values of $a_1^{\max}$ and w, and decreased the time required to transition between polarised states. Yet, a further reduction, to for example 0.00125, almost homogenised the response. This may be explained by the fact that since k_3 is the production rate of a_3, which locally inhibits a_3, reducing k_3 leaves the reaction–diffusion system with only one inhibitor, a_2, which might not increase fast enough to trigger pattern formation.

From these results, the parameter values of Exp. 11 will be used for chemotactic-driven directed cell migration. In this case, the system is able to adapt to a new signalling source and the strength and width of the peak ($a_1^{\max}$ and w) were among the largest. This shows the ability of the system to amplify the external signal. Fig. 4 shows the results of the simulation with such parameters. As can be seen, the system took around $t = 1.1$ to reach a stable polarised state. After that, at time 15 the signal was changed to the opposite direction and the system needed about $t = 150$ to develop the new polarised state. The transition from

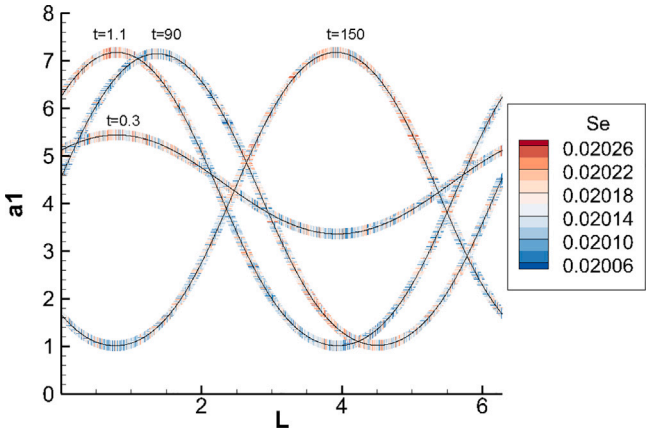

Fig. 4. Response of Meinhardt's model with parameters from Exp. 11. A stationary circle of radius 1 centred at $(0,0)$. The graph shows a_1 along the arc length at simulation times 0.3, 1.1, 90 and 150. The contour plot refers to s_e which started with a chemotactic signal at $(5,5)$ and changed to $(-5,-5)$ at time 15. As can be seen, the system went from a polarised state around $L = 1$ to another polarised state around $L = 4$ due to the change of the signalling-source point.

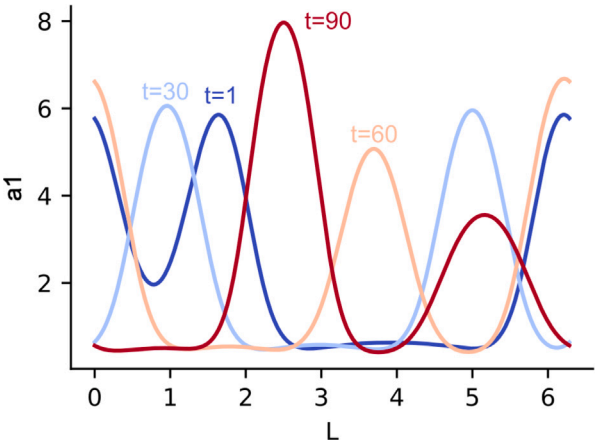

Fig. 5. Response of Meinhardt's model with parameters from Exp. 17. A stationary circle of radius 1 centred at $(0,0)$. The graph shows a_1 along the arc length at simulation times 1, 30, 60 and 90.

$t = 1.1$ to $t = 150$ occurred as a travelling wave as indicated by the results at time 90.

Similarly, the parameters of Exp. 17 will be used for spontaneous cell migration. As can be seen in Fig. 5, the competing peaks spontaneously change of orientation and are not affected by the external signal. This may represent a system of exploration of the environment.

5.2. Chemotactic-driven directed cell migration

Next, we analyse the impact of chemotactic cell migration as shown in Fig. 6. The simulation ran until $t = 205$ and the cell migrated towards the signalling-source points. We see the ability of the model to mimic migration pathways to specific locations and to adapt to the repositioning of the signalling sources. Fig. 6(a) shows the changes in shape of the cell and the position of its centroid as well as the a_b field. In this case, the domain conserved a round-like shape throughout the whole simulation. It must be noticed that the cell membrane—as well as the cytosol—rapidly polarised towards the first signalling-source point $(5,5)$. After the change in position of the signalling-source point, the cell polarised towards $(10,0)$ as expected. When the cell reached the source point, it continued to move and eventually passed over it. In consequence, the chemotactic signal became stronger at the cell rear,

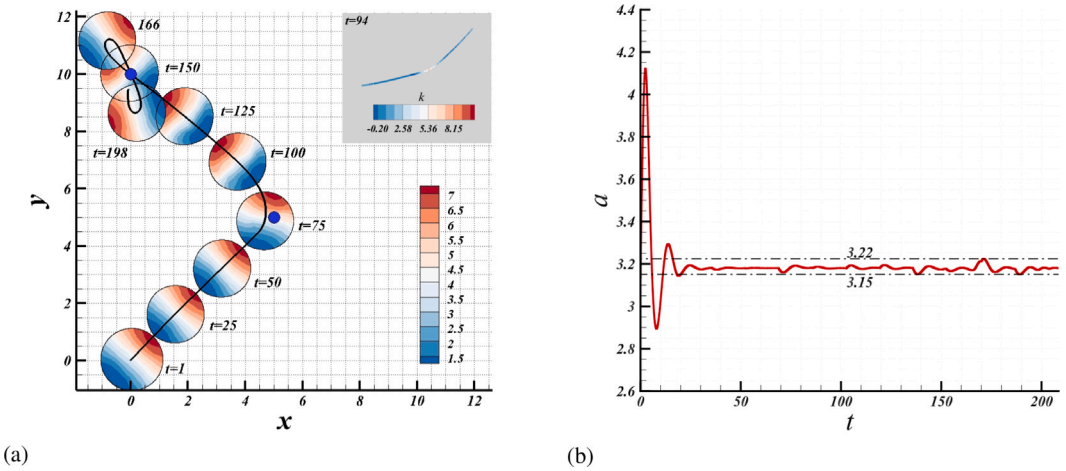

(a) (b)

Fig. 6. Results of chemotactic cell migration. (a) Results of the chemotactic-driven cell migration at $t = 1$, 25, 50, 75, 100, 125, 150, 166, 198 and the migration locus of the centroid. The colour map indicates the a_b field, the blue dots are the signalling-source points and the continuous and solid black line is the trajectory made by the cell centroid. The inner box indicates the curvature of the rear of the cell membrane at $t = 94$. The colour map refers to the signed curvature. (b) Evolution of cell area oscillating between 2.7 and 3.53.

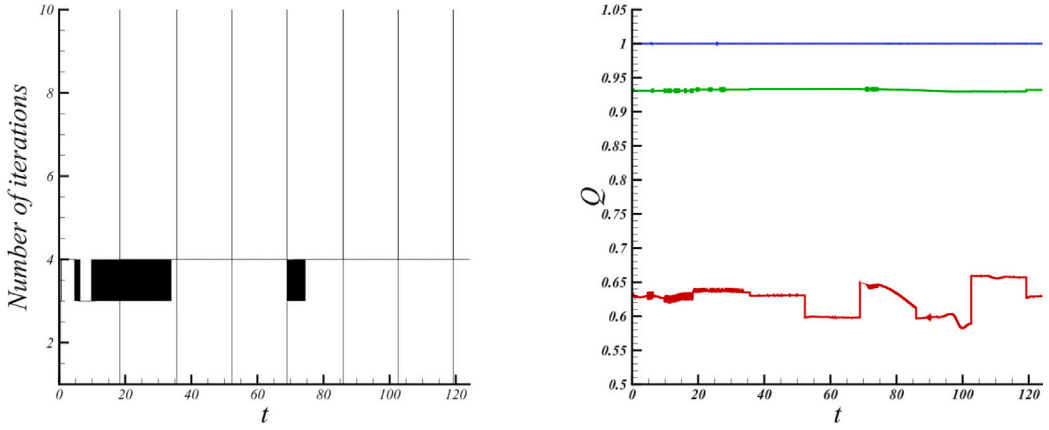

(a) (b)

Fig. 7. Report of mesh statistics and smoothing iterations at each step during chemotactic-driven cell migration. (a) Number of smoothing iterations. The vertical lines indicate re-meshing steps. (b) Mesh quality statistics. From top to bottom the curves indicate respectively the maximum, the average and the minimum qualities.

causing the membrane dynamics to reorient backwards. Therefore, as see in Fig. 6(a), after reaching the second point, the cell began to move around the source point due to this reorientation phenomenon.

Additionally, the simulation shows the appearance of a small protrusion at the rear, see the distribution of the signed curvature in Fig. 6(a). Fig. 6(b) shows the evolution of the cell area during the simulation. As can be seen, it varied strongly at the beginning, before $t = 20$, and then began to oscillate between time 3.15 and 3.22.

Finally, Fig. 7 shows the mesh quality (see Eq. (48)) and the positive impact of the mesh smoothing and re-meshing schemes. Fig. 7(b) shows, from top to bottom, the maximum, the average and the minimum element qualities, respectively, throughout the simulation. The maximum was 1 at every step which is in fact the maximum possible value. The average remained around 0.93—this is a high quality value and indicates that the mesh throughout the simulation was almost optimal. In contrast, the minimum quality fluctuated somewhat slightly with the lowest value at about 0.58 and the highest at about 0.68. In terms of the smoothing scheme, Fig. 7(a), in those cases where the algorithm was sufficient to deliver an acceptable mesh, 3 or 4 iterations were needed. Furthermore, it was not necessary to use the re-meshing scheme since the mesh was at optimal regularity (for example, for 18,000 time steps). Hence, the re-meshing algorithm was employed when it was absolutely necessary, thereby saving significantly on the computational costs and efficiency of the algorithm.

5.3. Spontaneous cell movement

Figs. 8 and 9 show the results for the case of spontaneous cell migration. In this case, the simulation was run until $t = 124$ and the cell migrated without any external signal or space dependent parameter. Fig. 8(b) shows the trajectory of the cell centroid that indicates zigzag migration and some directional persistence—rather than moving around $(0, 0)$ the cell moved towards $(0.6, -1.6)$. In Fig. 9, the shape and the a_b field is illustrated at $t = 1$, 25, 50, 75, 100, 124. Although the deformation of the domain is higher than in the previous case, it is noticeable how the round-like shape is still dominant. In addition, the commonly reported behaviour of Meinhardt's model can be seen, i.e., the appearance of two competing pseudopods (Meinhardt, 1999; Neilson et al., 2011; Elliott et al., 2012; Campbell et al., 2017)—nonetheless, in this simulation there is no external stimuli at all. Further, Fig. 8(a) shows that the area of the cell fluctuated much more, between 2.7 and 3.53 after $t = 20$.

Lastly, Fig. 10(b) describes the quality of the mesh throughout the simulation. Although the maximum quality was again 1, the average and the minimum qualities fluctuated more and reached lower values compared to the chemotactic case. Furthermore, Fig. 10(a) shows two stages. At the beginning, until about $t = 20$, the smoothing scheme was enough to deal with the mesh deformation. However, after $t = 20$, it was not enough and many more runs of the re-meshing scheme were needed.

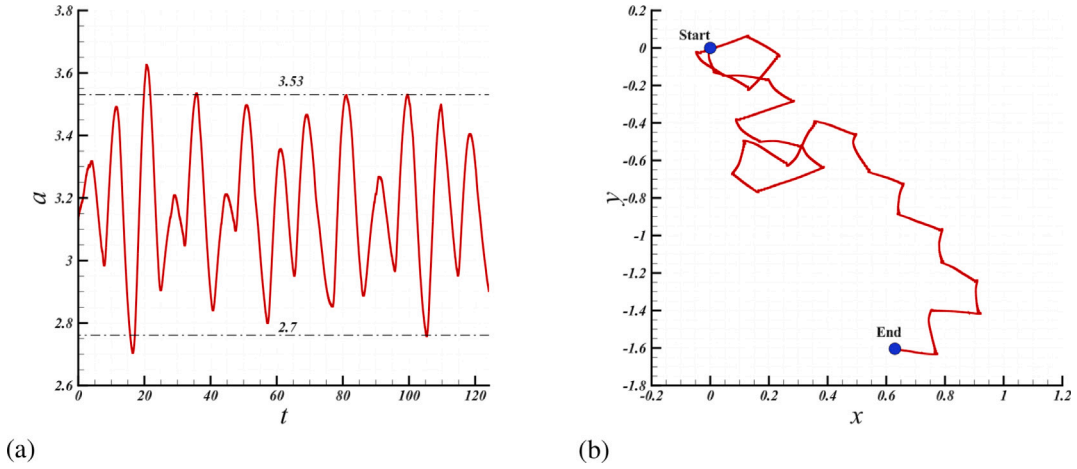

Fig. 8. Results of spontaneous cell migration. In (a), the cell area evolution during the simulation is presented which oscillates between 2.7 and 3.53. (b) illustrates the trajectory of the cell centroid.

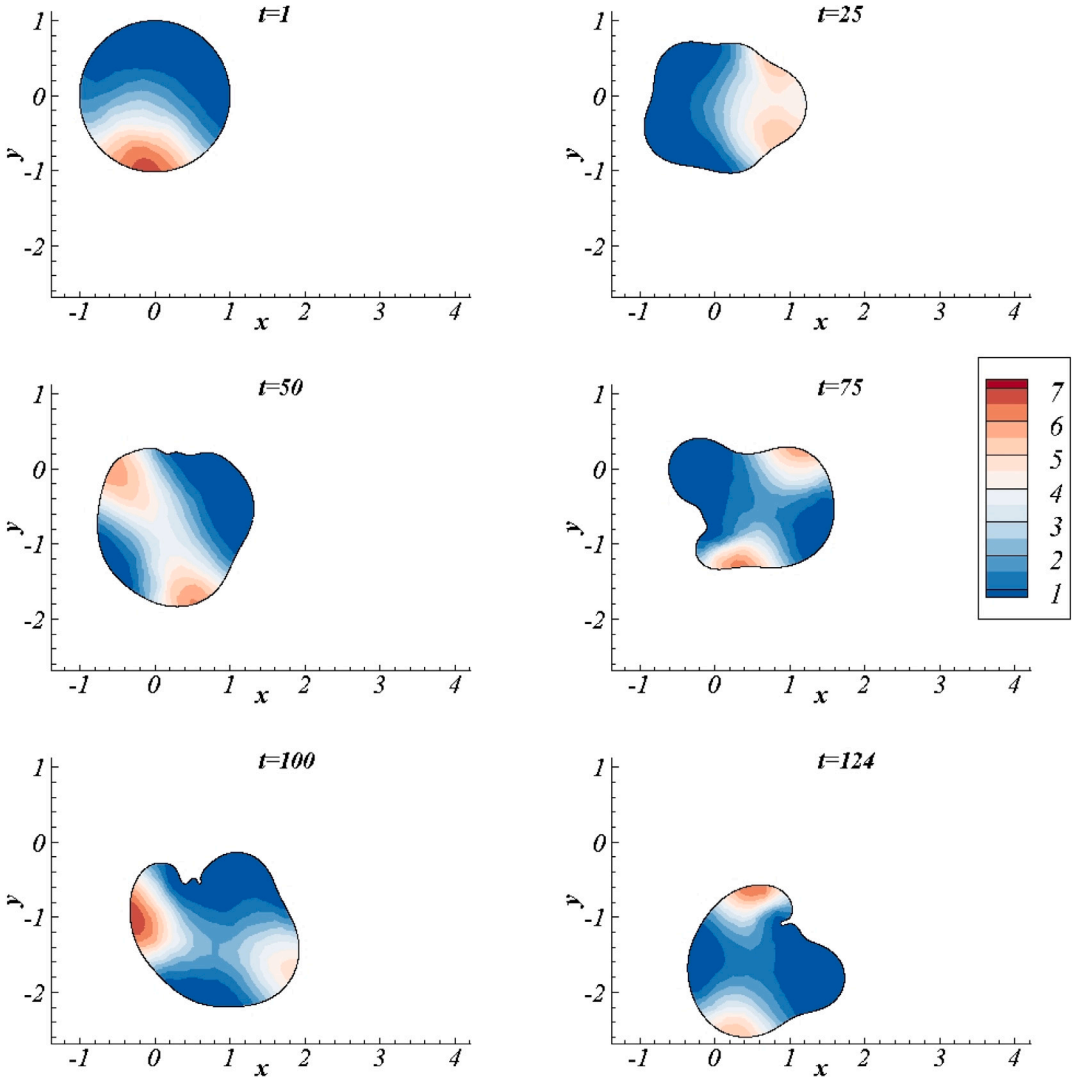

Fig. 9. Results of spontaneous cell migration. At $t = 1, 25, 50, 75, 100, 124$. The colour map indicates the a_b field.

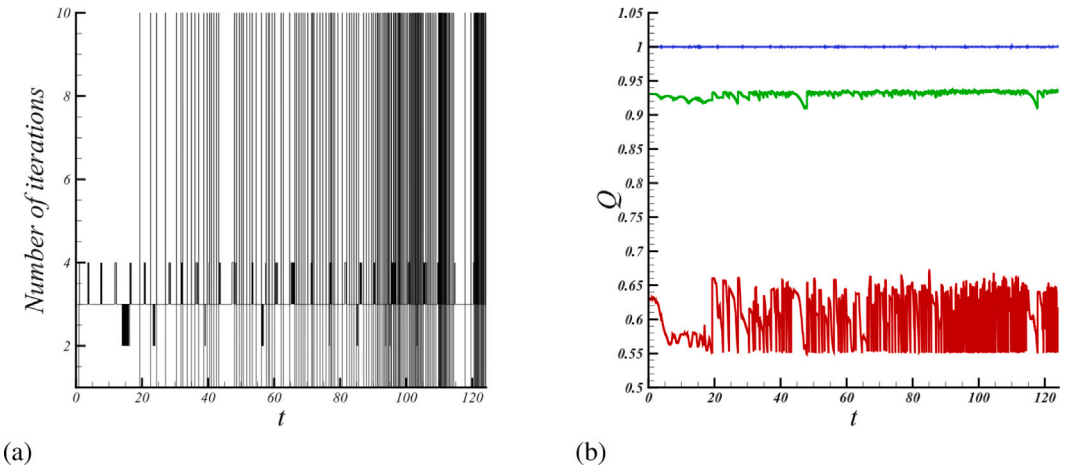

Fig. 10. Report of mesh statistics and smoothing iterations at each step in spontaneous migration. (a) Number of smoothing iterations. The vertical lines indicate a re-meshing step. (b) Statistics on the mesh regularity. From top to bottom the curves indicate respectively the maximum, the average and the minimum qualities.

6. Discussion

In this study, we have formulated a bulk-surface mechanobiochemical model for single cell migration during directed and spontaneous migration. The model couples mechanical properties describing the mechanical structure of the cytoskeleton with biochemical processes describing the spatiotemporal dynamics of the actomyosin molecules during the process of single cell migration. We then employed a novel bulk-surface moving-mesh finite element method to discretise the model in space. Standard finite differences in time allowed us to solve the resulting semi-discrete weak variational forms. By employing in a novel way, smoothing and re-meshing algorithms, we are able to exhibit computationally large cell deformations during migration. The computational framework allows us to access easily geometric, mechanical and biochemical properties which play a crucial role during the process of single cell migration. Not only are we able to exhibit cell migration pathways as observed experimentally, we are also able to compute and quantify geometric quantities such as the curvature, material and mesh velocities, area, speed, cell stiffness and the spatiotemporal distribution of the actomyosin molecules. This study significantly contributes to an emerging area of investigating the role of mechanics and biomolecular spatiotemporal dynamics during the process of single cell migration.

We briefly summarise here the computational modelling approach and its implementation. First, we saw that Meinhardt's model exhibits travelling-wave, chemotactic, and (ii) competing-peak, spontaneous behaviours, along the cell membrane. Although the dynamics of the leading edge varied from cell to cell, most cells have travelling actin waves (Allard and Mogilner, 2013; Kamps et al., 2020). These waves can appear locally or globally, depending on the cell and the extracellular environment on which it is migrating. For the case of chemotactically-driven migrating cells, the waves appear locally and help cells to avoid obstacles or reorientation or re-polarisation (Allard and Mogilner, 2013; Kamps et al., 2020). Fig. 11 illustrates this phenomenon in human breast cancer (MDA-MB-231 line). By following the arrows, which indicate the position of the leading edge, we appreciate the travelling wave from the top left to the bottom right of Fig. 11. This phenomenon, where the leading edge travels from one location to another, is successfully mimicked in the mechanobiochemical model in the presence of chemoattractant as illustrated in Fig. 6(a).

On the other hand, when cells move unsteadily the actin dynamics can include global travelling waves and the appearance of leading edges at different locations (Allard and Mogilner, 2013; Kamps et al., 2020). In Fig. 9, the spontaneous-migration case reproduces this type of kinetic dynamics, as also reported in Neilson et al. (2011), Elliott et al. (2012) and Campbell et al. (2017). Although the response is similar, in the case presented here, the parameters are all homogeneous, and thus, the kinetics is completely spontaneous—in Neilson et al. (2011), Elliott et al. (2012) and Campbell et al. (2017) the authors included a space-dependent chemotactic-signalling term. The dissimilarity in our chemotactic response therefore is due to the difference in parameters and the signalling term. Nonetheless, even though the model can reproduce chemotactic and spontaneous migration, it utilises different mechanisms depending on the different parameters in each scenario; thus, a further analysis of the model is required. It would be very interesting to find a set of parameters able to provide a local travelling wave in chemotactic migration as well as competing peaks in spontaneous migration.

In addition, our results show a marked round-like shape. This is common in amoeboid movement which is characterised by small or highly homogeneously distributed adhesion points and strong actomyosin-mediated contractility (Friedl and Alexander, 2011). In our mechanobiochemical model, the adhesion points are represented by the right-hand-side term of Eq. (13) which is space-independent. The contraction, dominated by $\lambda(t)$, is also homogeneous and therefore does not precisely model actomyosin-mediated contractility because λ is not polarised. Yet, it does contribute to maintain the round shape of the domain. Additionally, at time $t = 94$ for the chemotactic case, we see that the rear has a small protrusion (Fig. 6(a)) that can be also appreciated in Fig. 11. Although the protrusion in the simulation is not as large as the one observed in experiments (Gau and Roy, 2020), it indicates qualitative agreements with experiments. Lastly, while in chemotactic migration, the cell area achieved an almost steady state with a variation up to 2.5%, in spontaneous migration, this variation was larger, up to 14%. Therefore, our model predicts that in chemotactic migration, the cell adopts a protrusion-contraction regime in phase, in spontaneous migration, this regime is out of phase.

In the case of spontaneous migration, the trajectory (Fig. 8) exhibits zigzag turning and some directional persistence. Da Yang et al. (2011) describes this phenomenon for microglia cells from rats (PMG) and mice (MG5). In their experiments, cells were able to move freely, without external guidance and at a very low density, showing a tendency to advance in an almost linear straight direction followed by a sudden change in direction. Moreover, they determined a statistically significant zigzag pattern. In short, they showed that it is more likely that a microglia cell turn in the opposite direction of the previous turn than in the same direction. In other words, after turning with a positive angle it is more likely that the cell will turn with a negative angle and vice versa. In addition, they also reported a short-term directional persistence. This response of Meinhardt's model has been previously reported in Neilson et al. (2011) and Elliott et al. (2012).

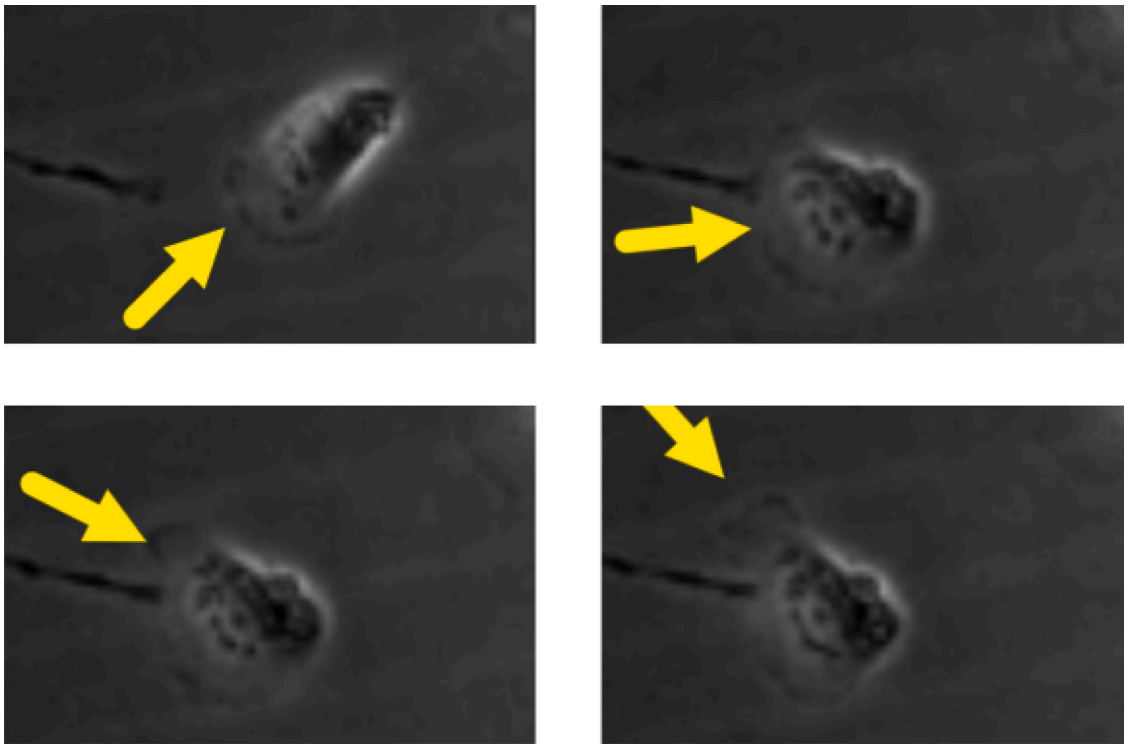

Fig. 11. Picture shots from a cell migration assay. Experiment using human breast cancer (MDA-MB-231 line) presented in Gau and Roy (2020) (permission given by Dr. Gau). The arrows point to the leading edge and show how it travels along the membrane.

7. Conclusions

In this work a computational modelling framework for the simulation of cell migration was introduced. The proposed framework is able to mimic both spontaneous and chemotactic or directed single cell migration with an appropriate selection of parameters. In addition, this computational framework deals with highly deforming domains by means of three algorithms: the de Boor's (1973) algorithm to equidistribute the boundary mesh, the Durand et al.'s (2019) algorithm to smooth the bulk mesh, and the Engwirda's (Engwirda, 2005, 2014) toolbox to remesh the domain when necessary. Furthermore, it is able to model and simulate bulk-surface processes that drive single cell migration on evolving two-dimensional domains.

In the current work, we presented a bulk-surface moving-mesh finite element method that allows the computation of a deforming domain for long periods of time and a simplified model for cell migration. In addition, we also improved the Durand et al.'s (2019) algorithm by combining it with the de Boor's (1973) algorithm. Durand et al. (2019) indicated that non-straight surface meshes, for example a circle, could not be smoothed with their method. Nevertheless, the de Boor's (1973) algorithm presented here, easily deals with such a drawback.

In short, our model considers a simplified biological system where the information goes from the membrane kinetics to the cytosolic kinetics that then leads to a mechanical response. Furthermore, as the mechanical response deforms the geometry—which at the same time affects the dynamics on the membrane and in the bulk—it indirectly affects the biochemical system. The membrane-protein dynamics are modelled with the Meinhardt's (1999) system for cell orientation, which can evolve in spontaneous competing peaks or in a forced and directed peak. This last response appears as an amplification of a space-dependent reaction rate that we compare to the activity of membrane receptors. The downstream effect from the plasma membrane to the cytoskeleton is given by a diffusion-depletion system that assumes that the actin-filament density close to the membrane is proportional to the activity of the membrane proteins. Thus, we considered that while the membrane activity affects the cytosolic activity, the latter does not affect the former. Finally, the model includes a mechanical response from the cytoskeleton activity. Mathematically, the mechanical model can be regarded as the product of: a local isotropic expansion due to the growth of actin filaments, a global contraction due to the area change, a homogeneous attachment to the substratum and curvature-dependent forces on the contour. Under the biological perspective, expansion and contraction occur as a consequence of the dynamics of the actin cytoskeleton and myosin proteins. In addition, focal adhesions and membrane tension are represented by elastic supports and curvature-dependent forces, respectively.

This study is a first step towards the formulation of a comprehensive predictive mechanobiochemical model for single cell migration where we couple mechanical and biochemical processes using the bulk (cytosol) and surface (cortex) spatiotemporal dynamics approach. Several improvements to the model are necessary if it is to be useful for experimental purposes. For example, the use of dummy parameters, the type of material behaviour, the lack of direct interpretation of the kinetic species, the required computational time, among others, need further studies.

Our modelling philosophy is that due to the complexity of the biological problem of single cell migration, the best way to build a robust cell migration simulator is to do adopt a modular approach. In other words, it is to develop each stage of the information flow separately and consistently with the biological theory. After that, combining the modules with proper cross-communication. Thus, future work could be focused on different modular aspects such as:

- more complex mechanical models, for example, the implementation of viscoelasticity or hyper-elasticity theories, to better describe the dynamics of the cytoskeleton,
- the development of biologically-inspired cytosolic and membrane kinetics and communication, for example, the formulation of bulk-surface PDEs where the variables directly represent specific molecules,

- different ways to model focal adhesions, for instance, since they do not appear everywhere and are constantly degraded, a stochastic equation could describe their location and a reaction equation for their strength, Ψ,
- a more discrete modelling of the cytosolic and membrane kinetics, for example, active and inactive GPCR's could be regarded as discrete entities able to modify the actin cytoskeleton at specific locations,
- the inclusion of the bending forces on the membrane,
- the use of experimental data to fit the model parameters, and
- introducing the extracellular matrix to study how single cells migrate through complex non-isotropic environments.

CRediT authorship contribution statement

David Hernandez-Aristizabal: Writing – original draft, Visualization, Validation, Methodology, Investigation, Formal analysis, Conceptualization. **Diego-Alexander Garzon-Alvarado:** Writing – review & editing, Supervision, Resources, Project administration, Methodology, Investigation, Funding acquisition, Formal analysis, Conceptualization. **Carlos-Alberto Duque-Daza:** Writing – review & editing, Supervision, Project administration. **Anotida Madzvamuse:** Writing – review & editing, Supervision, Project administration, Methodology, Funding acquisition, Formal analysis, Conceptualization.

Declaration of competing interest

None.

Acknowledgements

DHA was supported by the Universidad Nacional de Colombia, Colombia through resolutions: 405 of 2019, 051 and 0354 of 2020, and 166 of 2021. DHA thanks the University of Sussex for its hospitality during his one-month research visit to the UK. AM is partly supported by the EPSRC, United Kingdom grant number EP/J016780/1, the European Union Horizon 2020 research and innovation programme, UK under the Marie Sklodowska-Curie grant agreement No 642866, the Commission for Developing Countries, IMU; and the Simons Foundation. AM acknowledges the Royal Society Wolfson Research Merit Award (2016–2021) funded generously by the Wolfson Foundation, United Kingdom. This work (AM) was supported by the Canada Research Chair (Tier 1) in Theoretical and Computational Biology (CRC-2022-00147), the Natural Sciences and Engineering Research Council of Canada (NSERC), Discovery Grants Program (RGPIN-2023-05231), the British Columbia Knowledge Development Fund (BCKDF), Canada, Canada Foundation for Innovation – John R. Evans Leaders Fund – Partnerships (CFI-JELF), the British Columbia Foundation for Non-Animal Research, Canada, and the UKRI Engineering and Physical Sciences Research Council, United Kingdom (EPSRC: EP/J016780/1).

References

Acheson, D.J., 1990. Elementary Fluid Dynamics. Oxford University Press.

Ahmed, R.K., Abdalrahman, T., Davies, N.H., Vermolen, F., Franz, T., 2023. Mathematical model of mechano-sensing and mechanically induced collective motility of cells on planar elastic substrates. Biomech. Model. Mechanobiol. 22 (3), 809–824. http://dx.doi.org/10.1007/s10237-022-01682-2.

Alberts, B., Johnson, A., Lewis, J., Morgan, D., Raff, M., Roberts, K., Walter, P., 2015. The cytoskeleton. In: Molecular Biology of the Cell, sixth ed. Garland Science, New York, pp. 880–962.

Alhazmi, M., 2019. Exploring mechanisms for pattern formation through coupled bulk-surface PDEs in case of non-linear reactions. Int. J. Adv. Comput. Sci. Appl. 10 (3), 556–568. http://dx.doi.org/10.14569/IJACSA.2019.0100372.

Allard, J., Mogilner, A., 2013. Traveling waves in actin dynamics and cell motility. Curr. Opin. Cell Biol. 25 (1), 107–115. http://dx.doi.org/10.1016/j.ceb.2012.08.012.

Alt, W., Tranquillo, R.T., 1995. Basic morphogenetic system modeling shape changes of migrating cells, how to explain fluctuating lamellipodial dynamics. J. Biol. Systems 3 (4), 905–916.

Artemenko, Y., Lampert, T.J., Devreotes, P.N., 2014. Moving towards a paradigm: common mechanisms of chemotactic signaling in dictyostelium and mammalian leukocytes. Cell. Mol. Life Sci.: CMLS 71 (19), 3711–3747. http://dx.doi.org/10.1007/s00018-014-1638-8.

Aubry, D., Thiam, H., Piel, M., Allena, R., 2014. A computational mechanics approach to assess the link between cell morphology and forces during confined migration. Biomech. Model. Mechanobiol. 14 (1), 143–157. http://dx.doi.org/10.1007/s10237-014-0595-3.

Barreira, R., Elliott, C.M., Madzvamuse, A., 2011. Mathematical biology the surface finite element method for pattern formation on evolving biological surfaces. J. Math. Biol. 63, 1095–1119. http://dx.doi.org/10.1007/s00285-011-0401-0.

Barrett, J.W., Garcke, H., Nürnberg, R., 2020. Chapter 4 - parametric finite element approximations of curvature-driven interface evolutions. In: Bonito, A., Nochetto, R. (Eds.), Geometric Partial Differential Equations - Handbook of Numerical Analysis - Part I. Vol. 21, Elsevier, Amsterdam, Oxford, pp. 275–423. http://dx.doi.org/10.1016/bs.hna.2019.05.002.

Bartha, L., Eftimie, R., 2022. Mathematical investigation into the role of macrophage heterogeneity on the temporal and spatio-temporal dynamics of non-small cell lung cancers. J. Theoret. Biol. 549, 111207. http://dx.doi.org/10.1016/j.jtbi.2022.111207.

Bhattacharya, S., Iglesias, P.A., 2016. The regulation of cell motility through an excitable network. IFAC PapersOnLine 49 (26), 357–363. http://dx.doi.org/10.1016/j.ifacol.2017.03.001.

Brezzi, F., Falk, R.S., Donatella Marini, L., 2014. Basic principles of mixed virtual element methods. ESAIM Math. Model. Numer. Anal. 48 (4), 1227–1240. http://dx.doi.org/10.1051/m2an/2013138.

Buttenschön, A., Edelstein-Keshet, L., 2020. Bridging from single to collective cell migration: A review of models and links to experiments. PLOS Comput. Biol. 16 (12), e1008411. http://dx.doi.org/10.1371/journal.pcbi.1008411.

Camley, B.A., Zhao, Y., Li, B., Levine, H., Rappel, W.J., 2017. Crawling and turning in a minimal reaction-diffusion cell motility model: Coupling cell shape and biochemistry. Phys. Rev. E 95 (1), 1–13. http://dx.doi.org/10.1103/PhysRevE.95.012401, arXiv:1609.01764.

Campbell, E.J., Bagchi, P., Campbell, E.J., Bagchi, P., 2017. A computational model of amoeboid cell swimming a computational model of amoeboid cell swimming. Phys. Fluids 29, 101902:1–101902:16.

Campillo-Funollet, E., Venkataraman, C., Madzvamuse, A., 2019. Bayesian parameter identification for turing systems on stationary and evolving domains. Bull. Math. Biol. 81 (1), 81–104. http://dx.doi.org/10.1007/s11538-018-0518-z.

Chen, S., Liu, M., Huang, H., Zhang, Z., Li, B., Feng, X.-Q., Zhao, H.-P., 2020a. The relation between the collective motility and shapes of human cancer cells under heat stress. Appl. Phys. Lett. 116 (4), http://dx.doi.org/10.1063/1.5125833.

Chen, J., Weihs, D., Dijk, M.V., Vermolen, F.J., 2018a. A phenomenological model for cell and nucleus deformation during cancer metastasis. Biomech. Model. Mechanobiol. 17 (5), 1429–1450. http://dx.doi.org/10.1007/s10237-018-1036-5.

Chen, J., Weihs, D., Vermolen, F.J., 2018b. A model for cell migration in non-isotropic fibrin networks with an application to pancreatic tumor islets. Biomech. Model. Mechanobiol. 17 (2), 367–386. http://dx.doi.org/10.1007/s10237-017-0966-7.

Chen, J., Weihs, D., Vermolen, F.J., 2020b. Computational modeling of therapy on pancreatic cancer in its early stages. Biomech. Model. Mechanobiol. 19 (2), 427–444. http://dx.doi.org/10.1007/s10237-019-01219-0.

Cheng, Y., Othmer, H., 2016. A model for direction sensing in dictyostelium discoideum: Ras activity and symmetry breaking driven by a Gβ γ-mediated, Gα2-Ric8 – dependent signal transduction network. PLoS Comput. Biol. 12 (5), e1004900. http://dx.doi.org/10.1371/journal.pcbi.1004900.

Cusseddu, D., Edelstein-Keshet, L., Mackenzie, J.A., Portet, S., Madzvamuse, A., 2019. A coupled bulk-surface model for cell polarisation. J. Theoret. Biol. 481, 119–135. http://dx.doi.org/10.1016/j.jtbi.2018.09.008.

Cusseddu, D., Madzvamuse, A., 2022. Numerical investigations of the bulk-surface wave pinning model. Math. Biosci. 354, 108925. http://dx.doi.org/10.1016/j.mbs.2022.108925.

Da Yang, T., Park, J.S., Choi, Y., Choi, W., Ko, T.W., Lee, K.J., 2011. Zigzag turning preference of freely crawling cells. PLoS ONE 6 (6), e20255. http://dx.doi.org/10.1371/journal.pone.0020255.

de Boor, C., 1973. Good approximation by splines with variable knot. In: Numerical Solution of Differential Equations. In: Lecture Notes in Math., vol. 363, Springer, Dundee, pp. 12–20, 1974.

Devreotes, P., Horwitz, A.R., 2015. Signaling networks that regulate cell migration. Cold Spring Harbor Perspect. Biol. 7 (8), a005959. http://dx.doi.org/10.1101/cshperspect.a005959.

Diegmiller, R., Montanelli, H., Muratov, C.B., Shvartsman, S.Y., 2018. Spherical caps in cell polarization. Biophys. J. 115 (1), 26–30. http://dx.doi.org/10.1016/j.bpj.2018.05.033.

Durand, R., Pantoja-rosero, B.G., Oliveira, V., 2019. A general mesh smoothing method for finite elements. Finite Elem. Anal. Des. 158 (February), 17–30. http://dx.doi.org/10.1016/j.finel.2019.01.010.

Dziuk, G., Elliott, C.M., 2007. Finite elements on evolving surfaces. IMA J. Numer. Anal. 27 (2), 262–292. http://dx.doi.org/10.1093/imanum/drl023.

Dziuk, G., Elliott, C.M., 2013. Finite element methods for surface PDEs. Acta Numer. 22 (April), 289–396. http://dx.doi.org/10.1017/S0962492913000056.

Elliott, C.M., Ranner, T., 2013. Finite element analysis for a coupled bulk-surface partial differential equation. IMA J. Numer. Anal. 33 (2), 377–402. http://dx.doi.org/10.1093/imanum/drs022.

Elliott, C.M., Ranner, T., Venkataraman, C., 2017. Coupled bulk-surface free boundary problems arising from a mathematical model of receptor-ligand dynamics. SIAM J. Math. Anal. 49 (1), 360–397. http://dx.doi.org/10.1137/15M1050811.

Elliott, C.M., Stinner, B., Venkataraman, C., 2012. Modelling cell motility and chemotaxis with evolving surface finite elements. J. R. Soc. Interface 9 (June), 3027–3044. http://dx.doi.org/10.1098/rsif.2012.0276.

Elliott, C.M., Styles, V., 2012. An ALE ESFEM for solving PDEs on evolving surfaces. Milan J. Math. 80, 469–501. http://dx.doi.org/10.1007/s00032-012-0195-6.

Elowitz, M.B., Surette, M.G., Wolf, P.-E., Stock, J.B., Leibler, S., 1999. Protein mobility in the cytoplasm of escherichia coli. J. Bacteriol. 181 (1), 197–203. http://dx.doi.org/10.1128/jb.181.1.197-203.1999.

Engwirda, D., 2005. Unstructured mesh methods for the Navier-Stokes equations.

Engwirda, D., 2014. Locally-Optimal Delaunay-Refinement and Optimisation-Based Mesh Generation. (Ph.D. thesis). The University of Sydney.

Escribano, J., Chen, M.B., Moeendarbary, E., Cao, X., Shenoy, V., Garcia-Aznar, J.M., Kamm, R.D., Spill, F., 2019. Balance of mechanical forces drives endothelial gap formation and may facilitate cancer and immune-cell extravasation. PLoS Comput. Biol. 15 (5), e1006395. http://dx.doi.org/10.1371/journal.pcbi.1006395.

Espina, J.A., Marchant, C.L., Barriga, E.H., 2021. Durotaxis: the mechanical control of directed cell migration. FEBS J. 289 (10), 2736–2754. http://dx.doi.org/10.1111/febs.15862.

Farmer, A., Harris, P.J., 2023. A mathematical model of cell movement and clustering due to chemotaxis. J. Theoret. Biol. 575, 111646. http://dx.doi.org/10.1016/j.jtbi.2023.111646.

Ferreira, A.J.M., 2009. Plane stress. In: MATLAB Codes for Finite Element Analysis. Solid Mechanics and Its Applications In: Solid Mechanics and its Applications, vol. 157, Springer, Dordrecht, Dordrecht, pp. 143–152. http://dx.doi.org/10.1007/978-1-4020-9200-8.

Friedl, P., Alexander, S., 2011. Cancer invasion and the microenvironment: Plasticity and reciprocity. Cell 147 (5), 992–1009. http://dx.doi.org/10.1016/j.cell.2011.11.016.

Frittelli, M., Madzvamuse, A., Sgura, I., 2021. Bulk-surface virtual element method for systems of PDEs in two-space dimensions. Numer. Math. 147 (2), 305–348. http://dx.doi.org/10.1007/s00211-020-01167-3.

Frittelli, M., Madzvamuse, A., Sgura, I., Venkataraman, C., 2018. Numerical preservation of velocity induced invariant regions for reaction – diffusion systems on evolving surfaces. J. Sci. Comput. 77 (2), 971–1000. http://dx.doi.org/10.1007/s10915-018-0741-7.

Fuhrmann, J., Käs, J., Stevens, A., 2007. Initiation of cytoskeletal asymmetry for cell polarization and movement. J. Theoret. Biol. 249, 278–288. http://dx.doi.org/10.1016/j.jtbi.2007.08.013.

Gau, D., Roy, P., 2020. Single cell migration assay using human breast cancer MDA-MB-231 cell line. Bio-Protocol 10 (8), e3586. http://dx.doi.org/10.21769/BioProtoc.3586.

George, U.Z., Stéphanou, A., Madzvamuse, A., 2013. Mathematical modelling and numerical simulations of actin dynamics in the eukaryotic cell. J. Math. Biol. 66 (3), 547–593. http://dx.doi.org/10.1007/s00285-012-0521-1.

Giese, W., Eigel, M., Westerheide, S., Engwer, C., Klipp, E., 2015. Influence of cell shape, inhomogeneities and diffusion barriers in cell polarization models. Phys. Biol. 12 (6), 066014. http://dx.doi.org/10.1088/1478-3975/12/6/066014.

Goehring, N.W., Grill, S.W., 2013. Cell polarity: mechanochemical patterning. Trends Cell Biol. 23 (2), 72–80. http://dx.doi.org/10.1016/j.tcb.2012.10.009.

Gonçalves, I.G., Garcia-Aznar, J.M., 2021. Extracellular matrix density regulates the formation of tumour spheroids through cell migration. PLoS Comput. Biol. 17 (2), e1008764. http://dx.doi.org/10.1371/journal.pcbi.1008764.

González-Valverde, I., Semino, C., García-Aznar, J., 2016. Phenomenological modelling and simulation of cell clusters in 3D cultures. Comput. Biol. Med. 77, 249–260. http://dx.doi.org/10.1016/j.compbiomed.2016.08.019.

Han, S.J., Kwon, S., Kim, K.S., 2022. Contribution of mechanical homeostasis to epithelial-mesenchymal transition. Cell. Oncol. 45 (6), 1119–1136. http://dx.doi.org/10.1007/s13402-022-00720-6.

Harris, P.J., 2017. A simple mathematical model of cell clustering by chemotaxis. Math. Biosci. 294 (May), 62–70. http://dx.doi.org/10.1016/j.mbs.2017.10.008.

Heine, C.J., 2004. Isoparametric Finite Element Approximation of Curvature on Hypersurfaces University Freiburg, pp. 1–17. http://dx.doi.org/10.1093/imanum/drs037, Preprint.

Hobson, C.M., Stephens, A.D., 2020. Modeling of cell nuclear mechanics: Classes, components, and applications. Cells 9 (7), http://dx.doi.org/10.3390/cells9071623.

Holmes, W.R., Park, J., Levchenko, A., Edelstein-Keshet, L., 2017. A mathematical model coupling polarity signaling to cell adhesion explains diverse cell migration patterns. PLOS Comput. Biol. 13 (5), e1005524. http://dx.doi.org/10.1371/journal.pcbi.1005524.

Irgens, F., 2008. Theory of elasticity. In: Continuum Mechanics Springer Berlin Heidelberg, Berlin, Heidelberg, pp. 199–302. http://dx.doi.org/10.1007/978-3-540-74298-2.

Juma, V.O., 2019. Data-Driven Mathematical Modelling and Simulation of Rho-Myosin Dynamics (Ph.D. thesis). The University of Sussex.

Kamps, D., Koch, J., Juma, V.O., Campillo-Funollet, E., Graessl, M., Banerjee, S., Mazel, T., Chen, X., Wu, Y.-W., Portet, S., Madzvamuse, A., Nalbant, P., Dehmelt, L., 2020. Optogenetic tuning reveals rho amplification-dependent dynamics of a cell contraction signal network. Cell Rep. 33 (9), 108467. http://dx.doi.org/10.1016/j.celrep.2020.108467.

Koppenol, D.C., Vermolen, F.J., Niessen, F.B., van Zuijlen, P.P.M., Vuik, K., 2017. A biomechanical mathematical model for the collagen bundle distribution-dependent contraction and subsequent retraction of healing dermal wounds. Biomech. Model. Mechanobiol. 16 (1), 345–361. http://dx.doi.org/10.1007/s10237-016-0821-2.

Krause, M., Gautreau, A., 2014. Steering cell migration: lamellipodium dynamics and the regulation of directional persistence. Nat. Rev. Mol. Cell Biol. 15 (9), 577–590. http://dx.doi.org/10.1038/nrm3861.

Lewis, M.A., Murray, J.D., 1991. Analysis of stable two-dimensional patterns in contractile cytogel. J. Nonlinear Sci. 1, 289–311. http://dx.doi.org/10.1007/BF01238816.

Link, R., Jaggy, M., Bastmeyer, M., Schwarz, U.S., 2024. Modelling cell shape in 3D structured environments: A quantitative comparison with experiments. PLoS Comput. Biol. 20 (4), e1011412. http://dx.doi.org/10.1371/journal.pcbi.1011412.

Mackenzie, J., Rowlatt, C., Insall, R., 2021. A conservative finite element ALE scheme for mass-conservative reaction-diffusion equations on evolving two-dimensional domains. SIAM J. Sci. Comput. 43 (1), B132–B166. http://dx.doi.org/10.1137/19m1298585.

Madzvamuse, A., 2000. A Numerical Approach to the Study of Spatial Pattern Formation (Ph.D. thesis). University of Oxford.

Madzvamuse, A., Chung, A.H., 2016a. Analysis and simulations of coupled bulk-surface reaction-diffusion systems on exponentially evolving volumes. Math. Model. Nat. Phenom. 11 (5), 4–32. http://dx.doi.org/10.1051/mmnp/201611502.

Madzvamuse, A., Chung, A.H., 2016b. The bulk-surface finite element method for reaction–diffusion systems on stationary volumes. Finite Elem. Anal. Des. 108, 9–21. http://dx.doi.org/10.1016/j.finel.2015.09.002.

Madzvamuse, A., George, U.Z., 2013. The moving grid finite element method applied to cell movement and deformation. Finite Elem. Anal. Des. 74, 76–92. http://dx.doi.org/10.1016/j.finel.2013.06.002.

Madzvamuse, A., Maini, P.K., Wathen, A.J., 2005. A moving grid finite element method for the simulation of pattern generation by turing models on growing domains. J. Sci. Comput. 24 (2), 247–262. http://dx.doi.org/10.1007/s10915-004-4617-7.

Marsden, J.E., Chorin, A.J., 1993. A Mathematical Introduction to Fluid Mechanics Springer-Verlag.

McBeath, R., Pirone, D.M., Nelson, C.M., Bhadriraju, K., Chen, C.S., 2004. Cell shape, cytoskeletal tension, and rhoa regulate stem cell lineage commitment. Dev. Cell 6 (4), 483–495. http://dx.doi.org/10.1016/s1534-5807(04)00075-9.

Meinhardt, H., 1999. Orientation of chemotactic cells and growth cones: models and mechanisms. J. Cell Sci. 112, 2867–2874.

Miller, P.W., Fortunato, D., Muratov, C., Greengard, L., Shvartsman, S., 2022. Forced and spontaneous symmetry breaking in cell polarization. Nat. Comput. Sci. 2 (8), 504–511. http://dx.doi.org/10.1038/s43588-022-00295-0.

Morales, T., 2007. Chondrocyte moves: clever strategies?. Osteoarthr. Cartil. 15 (8), 861–871.

Mori, Y., Jilkine, A., Edelstein-Keshet, L., 2008. Wave-pinning and cell polarity from a bistable reaction-diffusion system Biophys. J. 94 (9), 3684–3697. http://dx.doi.org/10.1529/biophysj.107.120824.

Moure, A., Gomez, H., 2017. Phase-field model of cellular migration: Three-dimensional simulations in fibrous networks Comput. Methods Appl. Mech. Engrg. 320, 162–197. http://dx.doi.org/10.1016/j.cma.2017.03.025.

Moure, A., Gomez, H., 2019. Phase-field modeling of individual and collective cell migration Arch. Comput. Methods Eng. 28 (2), 311–344. http://dx.doi.org/10.1007/s11831-019-09377-1.

Murphy, L., Madzvamuse, A., 2020. A moving grid finite element method applied to a mechanobiochemical model for 3D cell migration Appl. Numer. Math. 158, 336–359. http://dx.doi.org/10.1016/j.apnum.2020.08.004, arXiv:1903.09535.

Murray, J.D., 2002. Mathematical Biology: I . An Introduction third ed. Springer, New York, Berlin, Heidelberg, pp. 1–505.

Murray, J.D., 2003. Mathematical Biology II: Spatial Models and Biomedical Applications third ed. Springer, New York, Berlin, Heidelberg, pp. 1–756.

Neilson, M.P., Mackenzie, J.A., Webb, S.D., Insall, R.H., 2011. Modeling cell movement and chemotaxis using pseudopod-based feedback Comput. Methods Sci. Eng. 33 (1), 1035–1057.

Nenninger, A., Mastroianni, G., Mullineaux, C.W., 2010. Size dependence of protein diffusion in the cytoplasm of escherichia coli J. Bacteriol. 192 (18), 4535–4540. http://dx.doi.org/10.1128/jb.00284-10.

Nenninger, A., Mastroianni, G., Robson, A., Lenn, T., Xue, Q., Leake, M.C., Mullineaux, C.W., 2014. Independent mobility of proteins and lipids in the plasma membrane of Escherichia coli Mol. Microbiol. 92 (5), 1142–1153. http://dx.doi.org/10.1111/mmi.12619.

Novak, I.L., Gao, F., Choi, Y.-S., Resasco, D., Schaff, J.C., Slepchenko, B.M., 2007. Diffusion on a curved surface coupled to diffusion in the volume: Application to cell biology J. Comput. Phys. 226 (2), 1271–1290. http://dx.doi.org/10.1016/j.jcp.2007.05.025.

Olayioye, M.A., Noll, B., Hausser, A., 2019. Spatiotemporal control of intracellular membrane trafficking by rho GTPases Cells 8 (12), 1478. http://dx.doi.org/10.3390/cells8121478.

Onsum, M.D., Rao, C.V., 2009. Calling heads from tails: the role of mathematical modeling in understanding cell polarization Curr. Opin. Cell Biol. 21 (1), 74–81. http://dx.doi.org/10.1016/j.ceb.2009.01.001.

Othmer, H.G., 2019. Eukaryotic cell dynamics from crawlers to swimmers Wiley Interdiscip. Rev.: Comput. Mol. Sci. 9 (1), e1376. http://dx.doi.org/10.1002/wcms.1376.

Peng, Q., Vermolen, F.J., Weihs, D., 2021. A formalism for modelling traction forces and cell shape evolution during cell migration in various biomedical processes Biomech. Model. Mechanobiol. http://dx.doi.org/10.1007/s10237-021-01456-2.

Peng, Q., Vermolen, F.J., Weihs, D., 2023. Physical confinement and cell proximity increase cell migration rates and invasiveness: A mathematical model of cancer cell invasion through flexible channels J. Mech. Behav. Biomed. Mater. 142, 105843. http://dx.doi.org/10.1016/j.jmbbm.2023.105843.

Rape, A.D., Guo, W.-h., Wang, Y.-l., 2011. The regulation of traction force in relation to cell shape and focal adhesions Biomaterials 32 (8), 2043–2051. http://dx.doi.org/10.1016/j.biomaterials.2010.11.044.

Rappel, W.J., Edelstein-Keshet, L., 2017. Mechanisms of cell polarization Curr. Opin. Syst. Biol. 3, 43–53. http://dx.doi.org/10.1016/j.coisb.2017.03.005.

Rätz, A., 2015. Turing-type instabilities in bulk–surface reaction–diffusion systems J. Comput. Appl. Math. 289, 142–152. http://dx.doi.org/10.1016/j.cam.2015.02.050.

Rätz, A., Röger, M., 2014. Symmetry breaking in a bulk–surface reaction–diffusion model for signalling networks Nonlinearity 27 (8), 1805–1827. http://dx.doi.org/10.1088/0951-7715/27/8/1805.

Ridley, A.J., Schwartz, M.A., Burridge, K., Firtel, R.A., Ginsberg, M.H., Borisy, G., Parsons, J.T., Horwitz, A.R., 2003. Cell migration: Integrating signals from front to back Science 302 (5651), 1704–1709. http://dx.doi.org/10.1126/science.1092053.

Schaks, M., Giannone, G., Rottner, K., 2019. Actin dynamics in cell migration Essays Biochem. 63 (5), 483–495. http://dx.doi.org/10.1042/ebc20190015.

Seetharaman, S., Etienne-Manneville, S., 2020. Cytoskeletal crosstalk in cell migration Trends Cell Biol. 30 (9), 720–735. http://dx.doi.org/10.1016/j.tcb.2020.06.004.

Séguis, J.-C., Burrage, K., Erban, R., Kay, D., 2012. Simulation of Cell Movement Through Evolving Environment: A Fictitious Domain Approach Technical Report, University of Oxford, pp. 1–36.

Shah, E.A., Keren, K., 2013. Mechanical forces and feedbacks in cell motility Curr. Opin. Cell Biol. 25 (5), 550–557. http://dx.doi.org/10.1016/j.ceb.2013.06.009.

Stéphanou, A., Chaplain, M.A., Tracqui, P., 2004. A mathematical model for the dynamics of large membrane deformations of isolated fibroblasts Bull. Math. Biol. 66 (5), 1119–1154. http://dx.doi.org/10.1016/j.bulm.2003.11.004.

Stéphanou, A., Tracqui, P., 2002. Cytomechanics of cell deformations and migration: from models to experiments C. R. Biol. 325, 295–308.

Turing, A., 1952. The chemical basis of morphogenesis Philos. Trans. R. Soc. Lond. B Biol. Sci. 237 (641), 37–72.

Uriu, K., Morelli, L.G., Oates, A.C., 2014. Interplay between intercellular signaling and cell movement in development Sem. Cell Dev. Biol. 35, 66–72. http://dx.doi.org/10.1016/j.semcdb.2014.05.011.

Vorotnikov, A.V., 2011. Chemotaxis: Movement , direction , control Biochemistry (Moscow) 76 (13), 1528–1555.

Wang, Y., Irvine, D.J., 2013. Convolution of chemoattractant secretion rate, source density, and receptor desensitization direct diverse migration patterns in leukocytes Integr. Biol. 5 (3), 481–494. http://dx.doi.org/10.1039/c3ib20249f.

Warner, H., Wilson, B.J., Caswell, P.T., 2019. Control of adhesion and protrusion in cell migration by Rho GTPases Curr. Opin. Cell Biol. 56, 64–70. http://dx.doi.org/10.1016/j.ceb.2018.09.003.

Yamada, K.M., Sixt, M., 2019. Mechanisms of 3D cell migration Nat. Rev. Mol. Cell Biol. 20, 738–752. http://dx.doi.org/10.1038/s41580-019-0172-9.

Zhao, J., Cao, Y., Dipietro, L.A., Liang, J., 2017. Dynamic cellular finite-element method for modelling large-scale cell migration and proliferation under the control of mechanical and biochemical cues: a study of re-epithelialization J. R. Soc. Interface 14 (129), http://dx.doi.org/10.1098/rsif.2016.0959.